Electronic Theses and Dissertations

Theses, Dissertations, and Major Papers

10-5-2017

Hydrodynamics of Buoyant Vortex Rings

Xueying Yan
University of Windsor

Hydrodynamics of Buoyant Vortex Rings

By

Xueying Yan

A Thesis
Submitted to the Faculty of Graduate Studies
through the Department of Mechanical, Automotive, and Materials Engineering
in Partial Fulfillment of the Requirements for
the Degree of Master of Applied Science
at the University of Windsor

Windsor, Ontario, Canada

Hydrodynamics of Buoyant Vortex Rings

by

Xueying Yan

APPROVED BY:

_____

N. Biswas
Department of Civil and Environmental Engineering

_____

G. Rankin
Department of Mechanical, Automotive and Materials Engineering

_____

R. Carriveau, Co-Advisor
Department of Civil and Environmental Engineering

_____

D.S-K. Ting, Co-Advisor
Department of Mechanical, Automotive and Materials Engineering

August 31, 2017

DECLARATION OF CO-AUTHORSHIP/PREVIOUS PUBLICATION

I hereby declare that this thesis incorporates material that is a result of joint research, as follows:

This thesis includes three original papers that have been previously published/submitted for publication in peer-reviewed journals/conferences, as follows:

Thesis Chapter	Publication title/full citation	Publication status*
Chapter 2	X.Y. Yan, R. Carriveau, D.S-K. Ting, Laminar to turbulent buoyant vortex ring regime in terms of Reynolds number, Bond number and Weber number, Journal of Fluids Engineering	Under review
Chapter 3	X.Y. Yan, R. Carriveau, D.S-K. Ting, Natural transportation: buoyant vortex rings, Energy and Natural Resources, Windsor, 2017.	Presented
Chapter 4	X.Y. Yan, R. Carriveau, D.S-K. Ting, Vortical flow structures behind a torus with an aspect ratio of three, Flow Measurement and Instrumentation	Under review

I am aware of the University of Windsor Senate Policy on Authorship and I certify that I have properly acknowledged the contribution of other researchers to my thesis, and have obtained written permission from each of the co-author(s) to include the above material(s) in my thesis.

I certify that, with the above qualification, this thesis, and the research to which it refers, is the product of my own work.

I certify that I have obtained a written permission from the copyright owner(s) to include the above published material(s) in my thesis. I certify that the above material describes work completed during my registration as graduate student at the University of Windsor.

I declare that, to the best of my knowledge, my thesis does not infringe upon anyone's copyright nor violate any proprietary rights and that any ideas, techniques, quotations, or any other material from the work of other people included in my thesis, published or otherwise, are fully acknowledged in accordance with the standard referencing practices. Furthermore, to the extent that I have included copyrighted material that surpasses the bounds of fair dealing within the meaning of the Canada Copyright Act, I certify that I have obtained a written permission from the copyright owner(s) to include such material(s) in my thesis.

I declare that this is a true copy of my thesis, including any final revisions, as approved by my thesis committee and the Graduate Studies office, and that this thesis has not been submitted for a higher degree to any other University or Institution.

ABSTRACT

A vortex ring is a torus-shaped vortex consisting of a region of fluid spinning around an imaginary axis line that forms a closed loop. It is an important phenomenon in animal kingdom and engineering applications. Birds and flying insects use buoyant vortex ring to glide higher altitudes; squid and jellyfish produce vortex rings during propulsion; vortex rings also participate in the blood flow through the human hearts. With the help of the vortex ring, animals can move fast and produce large thrust. In engineering, the Underwater Compressed Air Energy Storage (UWCAES) system uses surplus electricity to compress air into flexible accumulators (balloons) to store energy underwater. Balloons of stored compressed air may rupture when over-pressurized or pierced by a sharp object. This may generate a large-scale buoyant vortex ring, leading to water surface disruptions and undesirable waves. As a result, it is a necessity to study the hydrodynamics of a buoyant vortex ring.

This work presents three papers to have a better understanding of the fluid dynamics of a buoyant vortex ring. The first two papers focus on the flow behavior of a buoyant vortex ring and the third paper studies the vortex rings' influence on the ambient fluid (flow behind a buoyant vortex ring). The first paper characterized the formation conditions of a buoyant vortex ring and its transition behavior from a laminar to a turbulent vortex ring. It is followed by a paper investigating the flow characteristics of a buoyant vortex ring experimentally, including rising velocity, ring radius, relative core size, circulation and the energy development of a buoyant vortex ring. The final paper analyzed the wake of a vortex ring by simplifying that the core of a vortex ring is solid. This part of the work was conducted in a closed loop wind tunnel.

DEDICATION

I dedicate my thesis to my loving family for their unconditional love and support.

ACKNOWLEDGEMENTS

I would like to express my sincerest gratitude to Dr. Ting and Dr. Carriveau for their guidance and valuable suggestions during my M. A. Sc. program. Their encouragement and patience is essential throughout the past two years and help me grow.

I would also like to thank my committee members Dr. Rankin and Dr. Biswas for their contributions in providing their time and knowledge to keep me on track in my master's project. I also appreciate the technical assistance from Mr. Andy Jenner, Mr. Bruce Durfy and Ms. Kristie Pearce.

Finally, I would like to acknowledge my parents for providing me with financial support and continuous encouragement throughout my years of study. I would also express appreciation to my colleagues and friends, for their support and help. This accomplishment would not have been possible without them.

The Natural Science and Engineering Research Council of Canada has also supported this work.

A Turbulence & Energy Lab Research Project

TABLE OF CONTENTS

LIST OF TABLES

LIST OF FIGURES

CHAPTER 1 INTRODUCTION

1.1 Background and Motivation

Vortex rings, which are also called toroidal vortices, are a torus-shaped vortex consisting of a region of fluid spinning around an imaginary axis line that forms a closed loop (Figure 1. 1). Vortex rings are a basic fluid phenomenon exists in a wide range of biological, atmospheric, and engineering applications. They are naturally produced in different situations, and their beneficial properties have been applied to engineering applications.
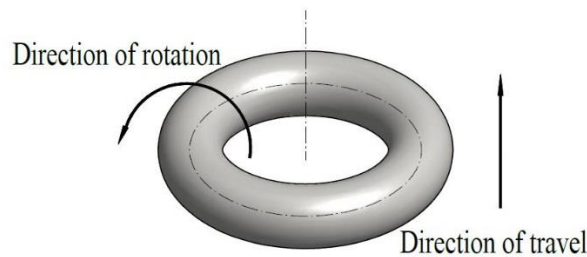
Figure 1. 1 Illustration of a vortex ring propagation.

Cephalopods, such as squid or octopus, use a jet propulsion method to swim underwater. They suck water into their muscular mantle cavity and then expel the water out quickly through a narrow siphon. The expelled water forms a sequence of the vortex rings behind cephalopods [1]. Due to the use of jet propulsion, the cephalopods can swim quickly and efficiently while making adjustments. Scientists are trying to study their flow control system to improve the performance of underwater vehicles. The investigations on the vortex rings can provide a better understanding of jet propulsion mechanism.

Birds and insects also produce vortex rings to generate enough lift for flying.

Investigating how they move and control their wings can help to build and exploit the micro-air-vehicles.

In biology, vortex rings are an optimized mechanism for blood transportation from the atria into the ventricles in the human heart [2]. Due to its high mass transportation efficiency, some researchers [3, 4] suggest that the vortex ring can be used as a medium to transport smoke into the atmosphere. This can reduce the necessity of tall chimneys, which can save money and avoid the potential structural failures.

In engineering, the Underwater Compressed Air Energy Storage (UWCAES) system [5] uses surplus electricity to compress air into flexible accumulators (balloons) to store energy underwater. Balloons of stored compressed air may rupture when over-pressurized or pierced by a sharp object. These balloons bursting underwater may also generate large-scale buoyant vortex rings, leading to water surface disruptions and undesirable waves. Thus, a thorough understanding of the fluid dynamics of a buoyant vortex ring is required before preventive measures can be properly implemented.

In nature, a vortex ring can also be produced by volcanic eruptions, the breath of dolphins, and cigarette smoking.

In summary, a vortex ring is a basic fluid structure in natural life. It is important to study the properties of a vortex ring to understand this fundamental fluid mechanics structure and further utilize it in practical applications.

1.2 Literature Review

A vortex ring can be characterized into buoyant and non-buoyant vortex rings depending on whether the core fluid density is lighter than the ambient fluid or not. The vortex ring structure was first mathematically analyzed by Helmholtz in 1958. After that,

researchers started to study the fluid dynamics of the vortex ring. The study on homogeneous (non-buoyant) vortex ring has been investigated thoroughly in the past 100 years, both numerically and experimentally. However, the study on a buoyant vortex ring has attracted limited attention.

One of the earliest studies of the buoyant vortex ring was conducted by Walters and Davidson [6]. They produced the bubble ring in the water and observed the radial expansion of the bubble ring. However, they did not make further quantitative measurements. After that, Turner [7] built an early analytical model of the buoyant vortex ring and explained that the radial expansion is due to the buoyancy force. He also conducted a series of experiments to verify his model. Afterwards, Pedley [8] did a theoretical analysis to study the stability of a buoyant vortex ring. He demonstrated that the velocity of a buoyant vortex ring decreases and the ring radius increases. He also predicted that the vortex ring has a finite lifetime and will eventually become unstable and break up due to the destabilizing influence of surface tension. Lundgren and Mansour [9] studied the flow behavior of vortex ring bubbles numerically and attributed the radial expansion to the generation of a downward Kutta-Joukowski lift. However, Joseph et al. [10] performed an analytical analysis under the assumption that the ambient fluid is viscous and the flow is irrotational. In contrast with the conclusion from Pedley [8], they stated that the vortex ring would finally achieve a steady state, at which the radius and velocity remain constant. Because the conclusion from Joseph et al. [10] is different from that predicted by Pedley [8], Cheng et al. [11] used lattice Boltzman simulation method, and Vasel et al. [12] used the bursting balloon experimental method to study the bubble ring rising in a viscous fluid. Both studies found that the bubble ring would finally become small spherical bubbles.

In addition, Bond and Johari [13] used PIV method study the development of a buoyant vortex ring and compared the buoyant vortex rings' phenomenon with that of a non-buoyant vortex ring with a similar Reynolds number. Han et al. [14] did series numerical simulations to study the formation of a bubble ring. They also studied the viscosity [15] and surface tension [16] effect on the bubble ring. Chen et al. [17] studied the transition behavior of a spherical bubble to a toroidal bubble.

Past studies provide valuable insights into the flow behavior of a buoyant vortex ring, both experimentally and numerically. However, many problems remain. For example, there is no literature on the differentiation of the laminar, transitional, and turbulent buoyant vortex ring regimes. Moreover, there are few studies on the energy development of a bubble ring. Furthermore, these studies have not explored the wake behind the vortex ring.

1.3 Thesis objective

The objective of the current study is divided into two parts: the flow behavior of a buoyant vortex ring and the wake structure of a buoyant vortex ring.

The study of the flow behavior of a buoyant vortex ring is conducted in a water tank. The movement of the buoyant vortex ring was captured by high-speed cameras. The following two goals were accomplished by analyzing the video:

1. Characterize the formation conditions of a buoyant vortex ring and its transition behavior from a laminar to a turbulent vortex ring.

2. Investigate the propagation dynamics of a buoyant vortex ring.

The core of the ring rotates while the vortex ring moves in the surrounding fluid. It is difficult to observe the wake of a buoyant vortex ring in a water tank. To simplify this problem, the author investigated the flow behind a solid core vortex ring. The wake

structure of a solid core vortex ring is conducted in the wind tunnel. By controlling the inlet wind velocity, the Reynolds number (based on the free stream velocity and the ring radius) of the solid core vortex ring is over the same range of Reynolds numbers as that of the buoyant vortex ring rising in water. Using the available facilities, the author has further scrutinized the wake behind a solid core vortex ring over the same range of Reynolds numbers as that of the buoyant vortex ring rising in water.

1.4 Organization of thesis

This thesis is arranged into five different chapters, each of which is briefly described below.

Chapter 1 introduces the background, a basic literature review on the buoyant vortex ring, the research objectives and the organization of the thesis.

Chapter 2 discusses the transition regime of the buoyant vortex ring experimentally. Based on the dimensional analysis results, the transition behavior of a buoyant vortex ring can be delineated regarding Bond number, Weber number and Reynolds number. This chapter also investigates the successful formation rate of a buoyant vortex ring at different orifice diameters of the apparatus.

Chapter 3 introduces the flow characteristics and the energy development of a buoyant vortex ring when it rises underwater.

Chapter 4 presents the flow structure of a solid core vortex ring with an aspect ratio of three at Reynolds numbers of 9×10^3, 1.2×10^4 and 1.5×10^4. This study details the vortical structures at 5, 7, 10 and 15 core diameters downstream of the torus. This chapter also scrutinizes the drag coefficient of the torus.

Chapter 5 summarizes the work in previous chapters and presents the options to

extend this work further.

References

[1] J.O. Dabiri, Optimal vortex formation as a unifying principle in biological propulsion, Annu. Rev. Fluid Mech. 41 (2009) 17-33.

[2] J. Töger, M. Kanski, M. Carlsson, S.J. Kovács, G. Söderlind, H. Arheden, E. Heiberg, Vortex ring formation in the left Ventricle of the heart: analysis by 4D flow MRI and Lagrangian coherent structures, Ann. Biomed. Eng. 40(12) (2012) 2652-2662.

[3] J.S. Turner, Intermittent release of smoke from chimneys, J. Mech. Eng. Sci. 2 (1960) 97-100.

[4] T. Fohl, Optimization of flow for forcing stack wastes to high altitudes, J. Air Pollut. Control Assoc. 17 (1967) 730-733.

[5] A. Pimm, S.D. Garvey, Underwater compressed air energy storage, in: Letcher T.M. (Ed.), Storing Energy: with Special Reference to Renewable Energy Sources, Elsevier, Oxford, 2016, pp. 135-139.

[6] J.K. Walters, J.F. Davidson, The initial motion of a gas bubble formed in an inviscid liquid, J. Fluid Mech. 17 (1963) 321-336.

[7] J.S. Turner, Buoyant vortex rings, Proc. Roy. Soc. Lond. A: Math. Phys. Eng. Sci. 239 (1957) 61-75.

[8] T.J. Pedley, The toroidal bubble, J. Fluid Mech. 32 (1968) 97-112.

[9] T.S. Lundgren, N.N. Mansour, Vortex ring bubbles, J. Fluid Mech. 224 (1991) 177-196.

[10] D.D. Joseph, T.Y. Liao, Potential flows of viscous and viscoelastic fluids, J. Fluids Mech. 265 (1994) 1-23.

[11] M.J. Cheng, T.T. Lim, Motion of a bubble ring in a viscous fluid, Phys. Fluids 25 (6) (2013) 067104.

[12] A.R. Vasel-Be-Hagh, R. Carriveau, D.S.-K Ting, A balloon bursting underwater, J. Fluid Mech. 769 (2015) 522-540.

[13] D. Bond, H. Johari, The impact of buoyancy on vortex ring development in the near field, Exp. Fluids 48 (2009), 737-745.

[14] W. Han, Z.Y. Yang, Y.M. Yang, Y. Hu, H.S. Zhang, Numerical investigation of the deformation mechanism of a bubble or a drop rising or falling in another fluid, Chin. Phys. B 17 (10) (2008) 3847.

[15] W. Han, Z.Y. Yang, Y.M. Yang, Y. Hu, H.S. Zhang, Viscosity effects on the behavior of a rising bubble, J. Hydrodyn. Ser. B 22 2010 81-89.

[16] W. Han, Z.Y. Yang, Y.M. Yang, Y. Hu, H.S. Zhang, Surface tension effects on the behavior of a rising bubble driven by buoyancy force, Chin. Phys. B 19 (2) (2010) 026801.

[17] L. Chen, S.V. Garimella, J.A. Reizes, E. Leonardi, The development of a bubble rising in a viscous liquid, J. Fluid Mech. 387 (1999) 61-96.

CHAPTER 2 LAMINAR TO TURBULENT BUOYANT VORTEX RING REGIME IN TERMS OF REYNOLDS NUMBER, BOND NUMBER AND WEBER NUMBER

2.1 Introduction

Vortex rings are a basic fluid dynamics phenomenon that is of both fundamental and practical importance. They can be generated by volcanic eruptions, the breath of aquatic creatures, and cigarette smoking. Vortex ring generation and propagation became an active research area in the last century, the early observations and experiments on ring vortices are detailed in a recent review by Fuentes [1]. Vortex rings can be categorized into buoyant and non-buoyant vortex rings depending on whether the core is less or equally as dense as the ambient fluid. Most of the research has been focused on single vortex rings that encompass a fluid that is the same as the ambient fluid. The investigation of these single-phase vortex rings may be divided into three phases: formation, propagation, and interaction with another surface. A chronological highlight summary of the research on vortex ring formation is given in Table 2. 1.

Table 2. 1 A chronological highlight of the vortex rings formation research.

1932	Lamb [2]	Proposed equations for the vortex ring parameters
1967	Chapman & Critchlow [3]	The best vortex rings formed from falling drops were generated from a spherical drop and changed from an oblate to prolate spheroid when in contact with the water surface.
1972	Maxworthy [4]	Used piston system to generate the vortex ring and studied the structure and stability of the vortex ring.
1979	Didden [5]	Established the slug model to describe the characteristics of the vortex ring generated by the

		piston system.
1992, 1995	Shariff & Leonard [6]; Lim & Nickels [7]	Provided a comprehensive investigation of the formation and dynamics of single-phase vortex rings.
1998	Gharib et al. [8]	Found the optimal formation time of the vortex ring, which determines the maximum circulation the vortex, could contain.
2007	Tang et al. [9]	Established a condition to produce effective vortical structures of synthetic-jet actuators to delay flow separation.
2009	Rosenfeld et al. [10]	Found the shape of the exit nozzle could also influence circulation and formation of the vortex ring.
2009	Dabiri [11]	Proposed an optimal vortex formation concept, which can potentially serve as a unifying principle to understand the diversity of solutions used to achieve propulsion in nature.
2013	Krieg & Mohseni [12]	Found the converging radial velocity ejected through the orifice would increase translational velocity compared with parallel jet flows with identical volume flux and nozzle diameter.
2014	Takagaki et al. [13]	Used direct numerical simulation (DNS) with a Level-Set method to investigate a drop impinging a free water surface. The generation and transport processes of the vortex rings are strongly affected by the angle of impingement of the drop.

Concerning the propagation phase of the vortex ring, the investigations were conducted in two vortex regimes, that is, based on whether the vortex ring is laminar or turbulent. A large part of the literature on the laminar vortex ring primarily focuses on an elegant instability in which azimuthal waves appear on a thin vortex core [4, 14]. Other groups study the turbulent vortex ring, with an emphasis on entrainment [15]. Glezer [16] constructed a transition map to reveal the relationship of boundary separation from laminar to turbulent forms of vortex rings based on the stroke ratio L/D. Other studies investigate

the interaction between the vortex ring and the free surface [17, 18]. In real life, a vortex ring is not perfectly axisymmetric, nor is the ring cross section perfectly circular. Falahatpisheha & Kheradvar [19] and Cheng et al. [20] proposed some concepts to measure these imperfections in the laboratory, where the motion of a piston is utilized to push a slug of fluid through a nozzle or orifice. The separation of the boundary layer at the edge of the opening causes the exiting fluid to roll into a vortex ring. Chen et al. [21] studied the evolution of a non-circular (elliptic) vortex ring.

Most of the previous studies, including those discussed above, are on non-buoyant vortex rings. There are very few studies focusing on buoyant vortex rings. Some of the original investigations on buoyant vortex rings were conducted experimentally by Walters and Davidson [22] starting in 1963. Turner [23] also proposed seminal theoretical studies on buoyant vortex rings. He modeled the fluid discharge from a steady supply of lighter fluid and described the flow behavior in both plumes and vortex rings. Since then, the studies on the properties of the buoyant vortex ring are divided into numerical and experimental parts. For the experimental investigations, Pedley [24] pointed out that the buoyant vortex ring has a finite lifetime. Shusser and Gharib [25] investigated the early formation of a vortex ring in a buoyant plume and found a buoyant vortex ring will pinch off the plume when the plume cannot provide enough energy to sustain a steady vortex ring. Pottebaum and Gharib [26] performed experiments and found that the pinch-off happened at a formation number (stroke ratio) around 4.4 to 4.9. Bond & Johari [27] found that a buoyant vortex ring becomes a thin core ring, whereas a non-buoyant vortex ring developed into a thick core ring after ring formation. Vasel et al. [28] investigated the propagation of a buoyant vortex ring experimentally. He found that as surface tension increases, the rise

velocity, and the circulation increase, while the expanding rate tends to constant values. In numerical investigations, Lundgren & Mansour [29] developed a semi-analytical model to predict the propagation of the buoyant vortex ring. Satti & Agrawal [30] made a computational model to simulate the buoyancy effects in a laminar starting jet. Gao & Yu [31] made a model for the pinch-off process of a vortex ring from its starting jet and found the results to be in good agreement with Shusser and Gharib's experiment results. A thermal vortex ring is an extreme example of a buoyant vortex ring; whose initial circulation is zero. Ganapathy [32] proposed a simple mathematical model to study the flow behavior of a weak thermal vortex ring. Chang [33] presented a method for computing the motion and decay of a large buoyant thermal.

To the authors' knowledge, there is no literature on the differentiation of the laminar, transitional, and turbulent buoyant vortex ring regimes. Through dimensional analysis, a correlation between Bond number, Weber number, and Reynolds number was proposed for a single buoyant vortex ring moving in a still Newtonian liquid. These three parameters could be used to delineate laminar and turbulent vortex ring regimes. This paper also studied the formation successful rate of a vortex ring at different orifice diameters and the propagation dynamics of a buoyant vortex ring.

2.2 Buoyant Vortex Rings

2.2.1 Vortex Ring Parameters

As shown in Figure 2. 1, R_{outer} is the outer radius of the vortex ring, R is the ring radius, and r_{core} is the vortex core radius.
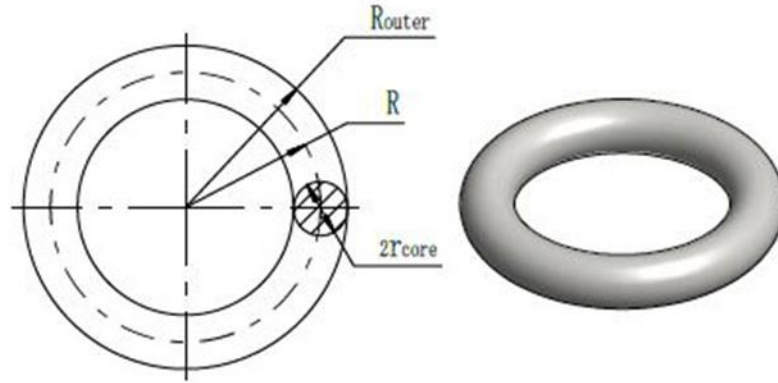
Figure 2. 1 Vortex ring parameters.

The volume of the vortex ring can be expressed as

$$\forall = \frac{4}{3}\pi r_0^3 = 2\pi R \times \pi r_{core}^2 \tag{2.1}$$

where r_0 is the equivalent spherical radius, which is equal to a perfect sphere enclosing the same volume of air as the vortex ring. As a result, the core radius equals to

$$r_{core} = \left(\frac{2r_0^3}{3\pi R}\right)^{1/2} \tag{2.2}$$

Knowing r_0 and R, the vortex core radius can be calculated. Therefore, the equivalent spherical radius and ring radius can be sufficient to determine the shape of the vortex ring.

2.2.2 Dimensional Analysis

The rising velocity of the vortex ring depends on the vortex ring characteristics (ring radius, core radius) and the properties of gas-liquid systems (air density, air viscosity, water density, water viscosity, and surface tension). A general equation for the rising velocity of the buoyant vortex ring can be expressed as a general function, G, of all relevant parameters

$$V=G (\mu_{air}, \rho_{air}, \mu_w, \rho_w, \sigma, g, r_{core}, R) \tag{2.3}$$

V=rising velocity, μ_{air}=air viscosity, ρ_{air}=air density, μ_w=water viscosity, ρ_w=water density σ=surface tension, g=gravity, r_{core} =core radius and R=ring radius.

From Eq. (2.2), we know that the core radius can be deduced by the equivalent

spherical radius r_0 and ring radius R. So the general function G shows in another form as

V=G (μ_{air}, ρ_{air}, μ_w, ρ_w, σ, g, r_0, R) $\qquad\qquad$ (2.4)

$\qquad$ There are nine variables (n=9) and three primary dimensions (MLT) so six pi terms

are needed. The dimensions of the variables are V = [L/t], μ_{air} = [M/(Lt)], ρ_{air} = [M/L^3], μ_w

= [M/(Lt)], ρ_w = [M/L^3], σ = [M/t^2], g=[L/t^2], r_0 = [L] and R = [L]. In this case, ρ_w, V and

R are selected as the repeating parameters. Using Buckingham Pi theorem, the pi terms are

deduced as follows:

$$\pi_1 = \frac{\mu_{air}}{\rho_w VR} \quad \pi_2 = \frac{\rho_{air}}{\rho_w} \quad \pi_3 = \frac{\mu_w}{\rho_w VR} \quad \pi_4 = \frac{\sigma}{\rho_w V^2 R} \quad \pi_5 = \frac{gR}{V^2} \quad \pi_6 = \frac{R}{r_0} \qquad (2.5)$$

$\qquad$ By combining the pi terms, two new pi terms are formed:

$$\pi_1' = \frac{\pi_1}{\pi_3} = \frac{\mu_{air}}{\mu_w} \qquad\qquad (2.6)$$

$$\pi_5' = \frac{\pi_5}{\pi_4 \times \pi_6^2} = \frac{\rho_w g r_0^2}{\sigma} \qquad\qquad (2.7)$$

$\qquad$ Then the pi terms π_1 to π_6 represents viscosity ratio, density ratio, Reynolds

number, Weber number, Bond number, and radius ratio, respectively.

$$\mu_r = \frac{\mu_{air}}{\mu_w} \qquad \rho_r = \frac{\rho_{air}}{\rho_w} \qquad Re = \frac{\rho_w VR}{\mu_w} \qquad We = \frac{\rho_w V^2 R}{\sigma} \qquad Bo = \frac{\rho_w g r_0^2}{\sigma} \qquad R_r = \frac{R}{r_0} \quad (2.8)$$

$\qquad$ Hence, the new relationship could be expressed as

$$F\left(\frac{\mu_{air}}{\mu_w}, \frac{\rho_{air}}{\rho_w}, Re, We, Bo, \frac{R}{r_0}\right) = 0 \qquad\qquad (2.9)$$

$\qquad$ For an air-water system, the density ratio, which is fixed in this study, can be neglected

as the air density is far smaller than the water density ($\rho_{air}/\rho_w \approx 0$). The viscosity ratio is also

constant and very large, and can also be neglected. As a result, the new function F is related

to four dimensionless numbers:

$$F\left(Re, We, Bo, \frac{R}{r_0}\right) = 0 \qquad\qquad (2.10)$$

$\qquad$ The radius ratio defines the shape of a vortex ring. The other three dimensionless

numbers are the fundamental parameters in analyzing two-phase fluid flows. Reynolds

number is the ratio of the inertial force to the viscous force and predicts the flow patterns. Weber number is the ratio of the inertial force to the surface tension. It can characterize the integrity of the bubble. Bond number measures the importance of the body force compared to the surface tension. It is used to characterize the shape of bubbles moving in a surrounding fluid.

The following sections show that the radius ratio can be a defining parameter between the laminar and turbulent vortex ring. The laminar vortex ring has a higher radius ratio compared to turbulent vortex ring. Based on Eq. (2.10), the radius ratio is the function of the Reynolds number, Weber number, Bond number.

$$\frac{R}{r_0} = F(Re, We, Bo,) \tag{2.11}$$

Therefore, these three parameters can also be used to delineate laminar and turbulent vortex ring regimes.

2.3 The Experiment

2.3.1 Apparatus

The experiment was conducted in a Plexiglas tank with dimensions of 0.8 m × 0.8 m × 2.4 m. The tank was filled with water up to 1.8 m above the membrane (aluminum) of the vortex generation chamber, as shown in Figure 2. 2. Experiments were conducted at room temperature under atmospheric pressure. Compressed air moved through a pressure regulator to a solenoid valve controlled by a programmable logic controller (PLC). When the solenoid valve opened, the air pushed the cap up against the force of the spring. Once the cap was lifted, compressed air rushed into the vortex generation chamber and burst out through the small nozzle (orifice) on a flexible membrane to generate the vortex ring.

All the experimental data were obtained photographically by a two-camera image

14

acquisition system. This system consisted of two cameras perpendicular to each other. One was positioned on the top of the tank; the resolution of this camera was 1920×1080, it had a frame rate of 30 fps; another camera (1280×720 resolution and 120 fps frame rate) was in front of the tank. This experiment also used two auxiliary backlights on the side and top respectively to outline the vortex ring clearly. For this experiment, five reference points were set at 0.3048-meter (1-foot) intervals in the front wall of the tank. By using a digital image processing method, the pixels of these reference points could be obtained. Then the pixels were correlated with the real position of the reference points, creating a pixel based reference frame for imaging measurements.
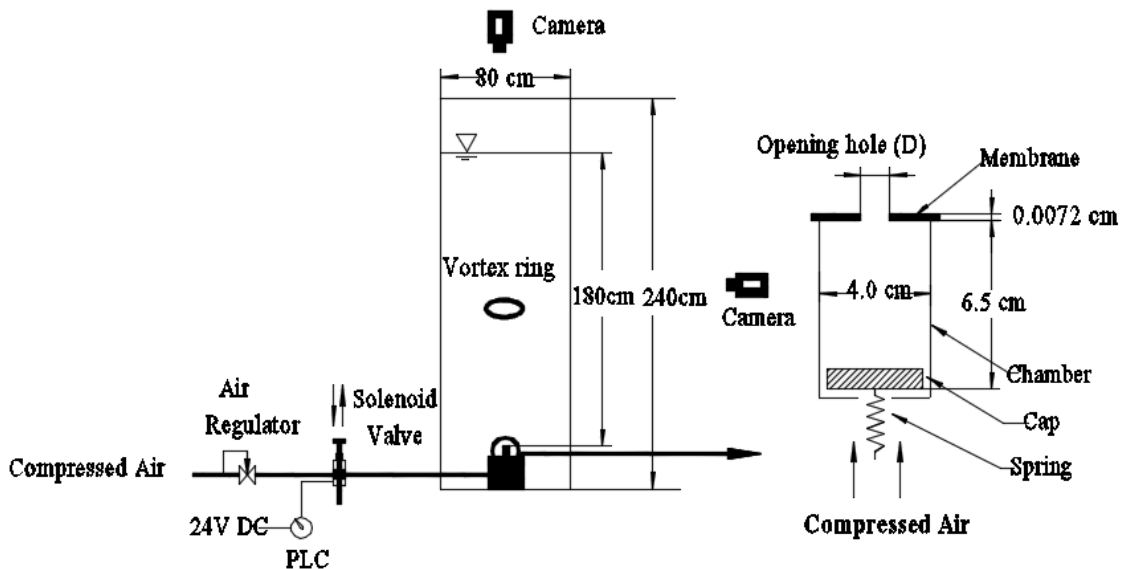
Figure 2. 2 Experimental apparatus.

2.3.2 Image Processing

MATLAB was utilized for image preprocessing, image binarization, image filling, and image edge detection to extract the vortex ring characteristics and convert the input image information into the desired digital information output. This process was automated; the program is shown in the flow chart in Figure 2. 3.

```
              ┌─────────────────────┐
              │    Current Image    │
              └─────────────────────┘
                         │
                         ▼
┌───────────────────────────────────┐      ┌──────────────────────┐
│     Subtract background image     │◄─────│   Background Image   │
└───────────────────────────────────┘      └──────────────────────┘
                         │
                         ▼
┌───────────────────────────────────┐
│      Choose the vortex ring area  │
└───────────────────────────────────┘
                         │
                         ▼
┌───────────────────────────────────┐
│   Use Median Filter Algorithm to  │
│        reduce noise [34]          │
└───────────────────────────────────┘
                         │
                         ▼
┌───────────────────────────────────┐
│    Do threshold operation and get │
│            binary image           │
└───────────────────────────────────┘
                         │
                         ▼
┌───────────────────────────────────┐
│          Do edge detection        │
└───────────────────────────────────┘
                         │
                         ▼
┌───────────────────────────────────┐
│   Use region props function [34] to │
│  get the parameters of the vortex ring │
└───────────────────────────────────┘
```
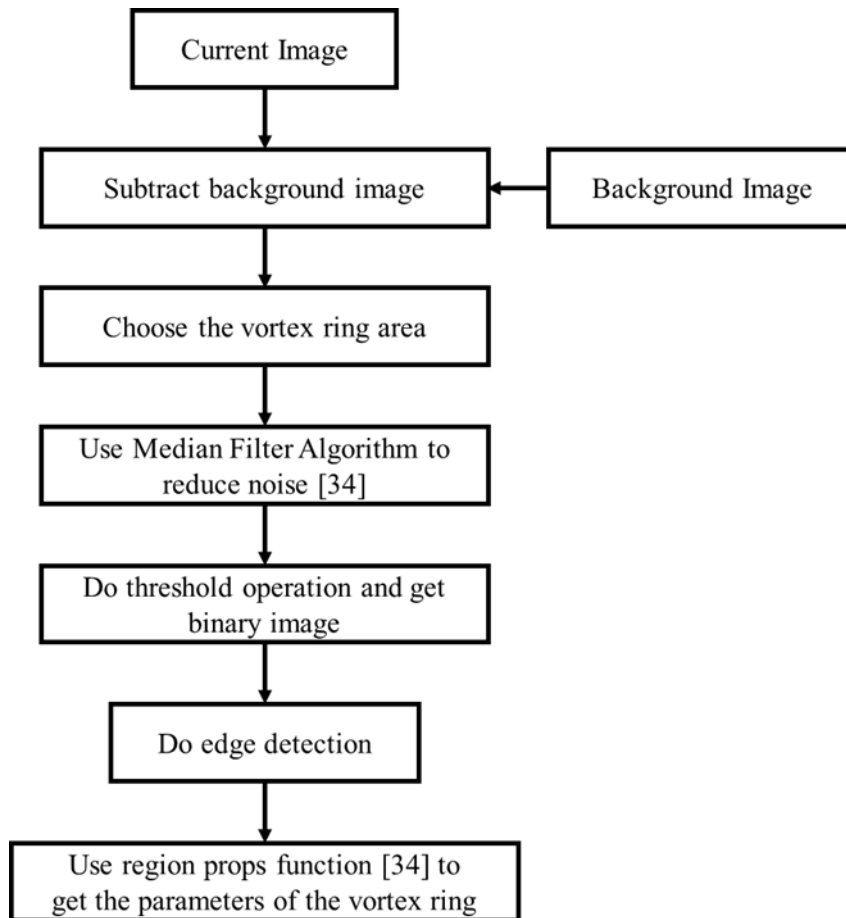
Figure 2. 3 Image processing flow chart.

The video containing the motion of the vortex ring was converted into a series of pictures. Then using a loop function in Matlab the pictures were processed frame by frame. First, a picture recorded the moment before the air rushes out of the membrane (no vortex ring) was selected as a background picture. Then the processing picture was subtracted from the background picture to delete the influence of the surrounding items around the vortex ring. This processed figure was a RGB image. Then the RGB figure was grayscaled, and a median filter was engaged (medfilt2) [34] to filter out the noise. Then OTSU Algorithm [34], named after its inventor Nobuyuki Otsu, was used to do computes a global threshold.

Then the grayscale image was converted into a binary image using 'im2bw' code [34].

The output image replaced all pixels in the input image with luminance greater than threshold with the value 1 (white) and replaced all other pixels with the value 0. That is, the value of the vortex ring pixel area equals 1, and the value of the background pixel area equaled zero. After that, the Canny method [34] was used to find the edge of the vortex ring in the binary image. Finally, Connected Region Area Measurement method (region props) [34] was used to label each area and calculate the characteristics of each labeled matrix so that the vortex ring characteristics, such as centroid and equivalent diameter, could be analyzed.

2.3.3 Vortex Ring Parameter Extraction

2.3.3.1 Centroid, Trajectory and Outer Radius of the Vortex Ring

In photography, perspective distortion is a transformation of an object and its surrounding area that differs significantly from what the object would look like with a normal focal length, due to the relative scale of nearby and distant features. Perspective distortion is determined by the relative distances at which the image is captured. To reduce this distortion, the camera in front of the tank was located far from the tank. The camera lens was directed to the middle part of the tank so that the side camera picture could reveal the full size of the vortex ring. After processing the video, the outline of the vortex ring in the side camera could be extracted. The centroid (x_c, z_c) of a vortex ring is the arithmetic mean position of all the points in the ring outline, where z_c was ring elevation. It was located at the corresponding time. The trajectory of the vortex ring was a mapped series of the centroids over time. The processed picture is shown in Figure 2. 4.

The outer diameter of the vortex ring equals the difference between the maximum x value and minimum x value of the outline points ($D_{outer}=x_{max}-x_{min}$); outer radius equals half

17

of the outer diameter ($R_{outer}=D_{outer}/2$).
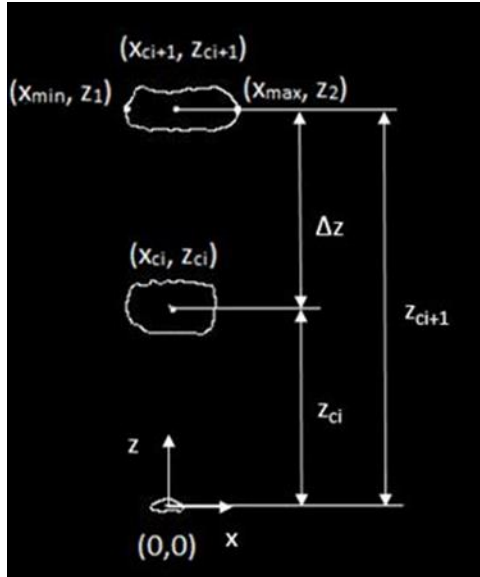
Figure 2. 4 Processed picture of the side camera.

2.3.3.2 Rising Velocity

The rising velocity of the vortex ring is

$$V = \frac{z_{ci+1} - z_{ci}}{\Delta t}$$
(2.12)

Where z_{ci} is the coordinate of the successive positions of the centroid of the vortex

ring, and Δt is the time interval between two successive pictures. In this paper, the time

interval is 1/30 s.

2.3.3.3 Vortex Ring Radius and Core Radius

The video of the top camera also repeated previous image processing progress. After

edge detection, two circular-shaped rings were obtained. The 'regionprops' function of

Matlab was used to estimate the center and radius of these two circular objects; this

information was engaged to plot circles on the image. The processed picture is shown in

Figure 2. 5. Then the outer diameter and inner diameter of the vortex ring can be deduced.

However, the top camera was not able to reveal the true dimensions of the vortex ring given

that the vortex ring appears big when near and small when far. Subsequently, some translation was conducted. Of course, the radius ratio of inner and outer circle ($r_{ratio}=D_{inner}/D_{outer}$) still revealed the actual radius ratio as inner and outer radius both changed with the distance.

Figure 2. 5 Processed picture of the top camera.

The videos of the top and side cameras were synchronized at the moment the air just rushed out of the membrane. Simultaneously, the side and top cameras recorded the same vortex ring outline. Thus, the outer radius recorded by the side camera, and the radius ratio recorded by the top camera represented the outer radius of the vortex ring and the radius ratio at this time. As a result, core radius and vortex ring radius could be calculated by the following equations:

$$r_{core} = \frac{(1-r_{ratio}) \times R_{outer}}{2} \tag{2.13}$$

$$R = R_{outer} - r_{core} \tag{2.14}$$

2.3.3.4. Equivalent Spherical Radius

Derived from Eq. (2.1), the equivalent spherical radius r_0 equals to

$$r_0 = \sqrt[3]{\frac{3\forall}{4\pi}} \tag{2.15}$$

The dimensions of length, time, velocity and force are normalized using r_0, $(r_0/g)^{1/2}$, $(gr_0)^{1/2}$ and gr_0^3 respectively, where g is the gravitational acceleration and r_0 is the equivalent spherical radius.

The details of the Matlab program are shown in Appendix B.

19

2.3.4 Experiment Details

This paper is divided into three investigations: the formation, propagation, and transition regime of the vortex ring.

- Formation: Test four orifice diameters to see which one has the highest rate of success with respect to generating the buoyant vortex ring.

- Propagation: For investigating the vortex ring parameters, such as rising velocity and ring radius, the Bond number was chosen as an independent variable to distinguish the vortex ring. The results were reported for Bond numbers 30 ± 8, 90 ± 12, 137 ± 15, 239 ± 13, 302 ± 20, and 379 ± 17 respectively with the compressed air pressure varied from 180 kPa to 300 kPa, over a duration of 0.1 s of the solenoid valve. Given uncertainties were obtained from the standard deviation of ten runs of the experiment at a 95% confidence level.

- Transition regime: Study the transition regime in terms of Bond number, Reynolds number and Weber number. These three parameters are controlled by using different initial volumes and velocity of the vortex rings; which is achieved by using different compressed air pressure and valve opening time. In addition, as the vortex ring rises, the radius ratio also changes. The experiment was conducted at air pressure from 180 kPa to 300 kPa with two opening times of the PLC (0.1s, 0.2s).

2.4. Results and Discussion

2.4.1 Vortex Ring Formation

The vortex ring forms through the separation of vortex sheets at the edge of the membrane body. In the current study, the separated flow is produced by using air pressure to push air through the orifice. When the air starts to go through the chamber, a flow

emanating from the orifice develops outside the membrane. The initially thin boundary layer of the air separates at the orifice, and the vortical air rolls up into a vortex ring, which moves upstream due to buoyancy and initial kinetic energy [5].

2.4.1.1 The Ratio of Chamber Diameter to Orifice Diameter

The geometry of the orifice can influence the formation potential of the buoyant vortex ring. The ratio of the chamber diameter to orifice diameter can be used as a parameter to influence the formation of the vortex ring [6]. Our work investigated four ratios (5.1, 4.2, 3.6, and 3.1). Each experimental condition was tested thirty times. The formation outcomes of the vortex ring at different ratios of the chamber diameter (D_c) to orifice diameter (D) were recorded in Table 2. 2.

As seen from Table 2. 2, $D_c/D=3.1$ cannot produce a vortex ring at lower air pressures (180 kPa, 0.1s, 180 kPa, 0.2 s and 200 kPa, 0.2s) and $D_c/D=5.1$ cannot form the vortex ring at higher air pressure (0.2 s, 240 kPa) compared to the formation range of $D_c/D=3.6$ or 4.2. Therefore, $D_c/D=3.6$ or 4.2 has a wider formation range. The he suitable ratio of the chamber diameter to orifice diameter is 3.6-4.2.

Table 2. 2 Formation probability of buoyant vortex ring.

Ratio of chamber diameter to orifice diameter D_c/D		5.1 D=7.9 mm	4.2 D=9.5 mm	3.6 D=11.1 mm	3.1 D=12.7 mm
Time (s)	Pressure (kPa)	Successful rate	Successful rate	Successful rate	Successful rate
	140	0	0	0	0
	160	0	0	0	0

	180	17%	30%	27%	0
0.1	200	27%	30%	56%	35%
	220	18%	21%	38%	25%
	240	18%	15%	15%	15%
	260	15%	7%	21%	10%
	280	10%	12%	13%	11%
	300	10%	10%	25%	25%
	180	0	20%	15%	0
0.2	200	10%	0	14%	0
	220	11%	10%	20%	27%
	240	0	18%	33%	30%

2.4.2 The Vortex Rings' Propagation

2.4.2.1 Entrance Area

The entrance area is the region where the bulk of air bubble forms a buoyant vortex ring. Figure 2. 6 shows the dimensional velocity trajectory of the vortex ring at different Bond numbers. The velocity of the vortex ring shows a reducing tendency when the height increases. For low Bond numbers, the velocity decreases smoothly. For high Bond numbers, the velocity fluctuates as the vortex ring rises. The graph shows a decreasing trend. If the elevation is below 0.8 m, the velocity fluctuates notably without any tendency to decrease, and the shape of the vortex ring changes dramatically, especially for the higher Bond numbers. After that, the velocity will decrease, and the ring radius will show a concentric circular shape. This may be because the elevation below 0.8 m is the entrance part where the outlet air is just forming the vortex ring. When the vortex ring is formed, an azimuthal

22

disturbance will occur around the vortex core during its rise. This azimuthal wave makes the ring radius of the vortex ring fluctuate [4]. When the azimuthal wave had a large amplitude, it led to the vortex ring breaking down on issue from the nozzle. After 0.8 m, the azimuthal wave became stable, so the velocity and radius fluctuated slightly. The velocity of the higher Bond number fluctuated more as it rose owing to the large azimuthal wave amplitude associated with the higher Bond number.
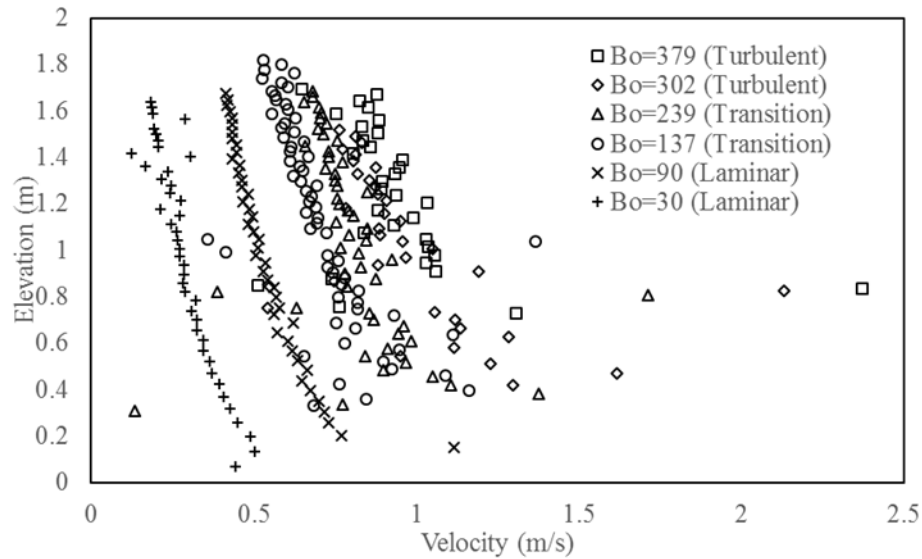
Figure 2. 6 Elevation versus velocity at different Bond numbers.

2.4.2.2 Definition of Laminar and Turbulent Buoyant Vortex Rings

As discussed, the vortex ring would break down into turbulent vortex rings due to the large amplitude azimuthal disturbances. In our study, the azimuthal wave led to the rings fluctuating significantly early in the life of the turbulent cases. By the time the ring had reached our observation zone (0.8 m above the membrane elevation), they were largely identifiable as laminar or turbulent. The difference between what we observed as laminar or turbulent vortex rings are shown in Figure 2. 7.

For the laminar vortex ring, the vorticity of the rotating core is small, so the surface

of the vortex ring remains smooth as it goes up and the cross-section decreases. Given the reduced azimuthal wave magnitude, the ring retained a very circular shape as observed from the top.

For the turbulent vortex ring, the core of the vortex ring rotated violently, such that the surface of the vortex ring only remained ring-shaped but not smooth. The cross section of the vortex ring rotated intensely and developed a wavy unstable shape. The difference between these types was easily distinguished by the video captured by both cameras.

For the present study, when Bond number was equal to 30 and 90, the experiment was only able to generate the laminar vortex ring. When the Bond number was equal to 137 and 239, the experiment could form either laminar or turbulent vortex rings. This seemed to indicate a transition zone. When the Bond number was equal to 302 and 379, the experiment could only produce the turbulent vortex ring.
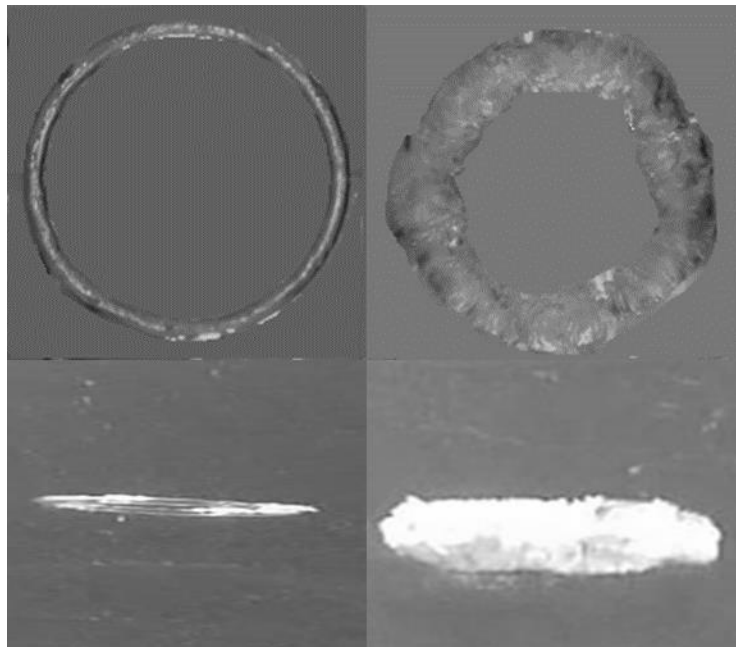
Figure 2. 7 Laminar versus turbulent buoyant vortex ring (up: top view, bottom: side view).

2.4.2.3 Rising Velocity

Figure 2. 8 describes the dimensionless velocity of the vortex ring at different Bond numbers. The picture illustrates that initially velocity increases as Bond number increases. However, when Bond number equals 137, dimensionless velocity will no longer increase and the dimensionless velocity versus dimensionless time curves of different Bond numbers will coincide with each other.
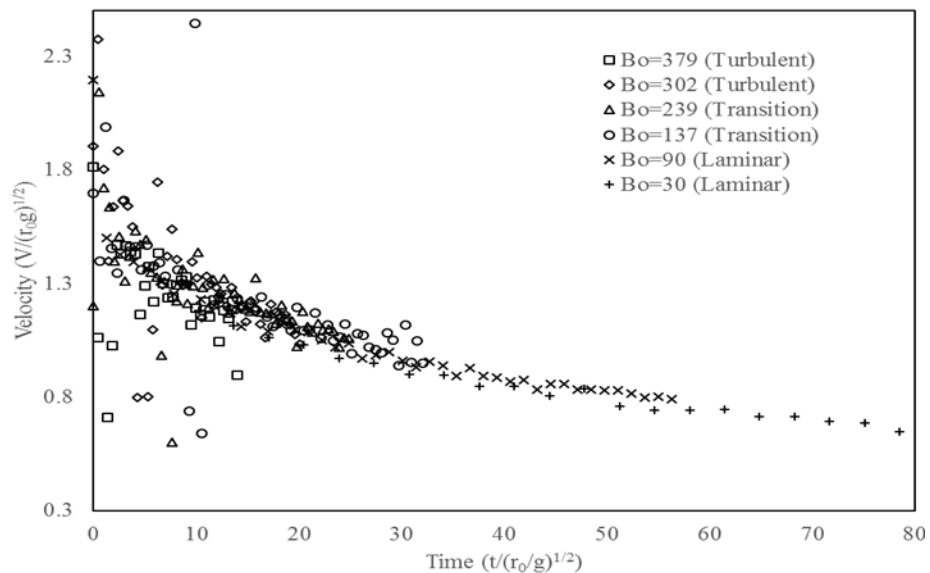
Figure 2. 8 Dimensionless velocity versus dimensionless time at different Bond numbers.

The vortex ring is generated by the ejection of compressed air through an orifice to the water tank. The initial energy of the vortex ring is the compressed air kinetic energy, driven by the pressure and the potential energy of the air. The greater the air volume, the more potential energy the vortex ring will have. Here the Bond number is controlled by increasing the air pressure. As a result, the higher Bond number leads to a higher kinetic energy and potential energy. The dimensionless velocity will increase with the Bond number. However, when that Bond number equals to 137, the vortex rings reach a transitional regime. The vortex ring will become turbulent and entrainment becomes

prominent. The larger the Bond number, the greater the fluid entrainment. The velocity of the vortex ring depends on the distribution and amount of the vorticity. Although the initial energy is larger for the higher Bond number, this energy will redistribute itself over a larger area. Therefore, the dimensionless velocity will no longer increase with the Bond number when the vortex ring reaches the transition regime.

It also can be observed that the dimensionless velocity decreases with time at a specific Bond number. This may be because of the drag of the water, as the drag coefficient is related to the velocity, i.e. $C_D = f(V^2)$. At the outset, when the vortex ring is moving with a higher initial speed, the drag on the vortex ring is larger than its buoyancy force. Consequently, the vortex ring will decelerate. As velocity decreases, the drag of the vortex ring will also decrease. When it equals the buoyancy force, the vortex ring will remain steady. This could be seen at lower Bond numbers, when Bo=30 and Bo=90, the velocity decreased and finally reached a terminal velocity. However, for larger Bond numbers, the initial velocity is too large, and the vortex ring does not have enough time to reach the steady state.

2.4.2.4 Radius

The effect of the surface tension on the vortex ring's radius is illustrated in Figure 2. 9. From the picture, we observe that the dimensionless radius decreases with Bond number. This is because the Bond number is the ratio of body force to surface tension. The lower Bond number represents higher surface tension. The higher surface tension prevents the bubble ring from expanding.
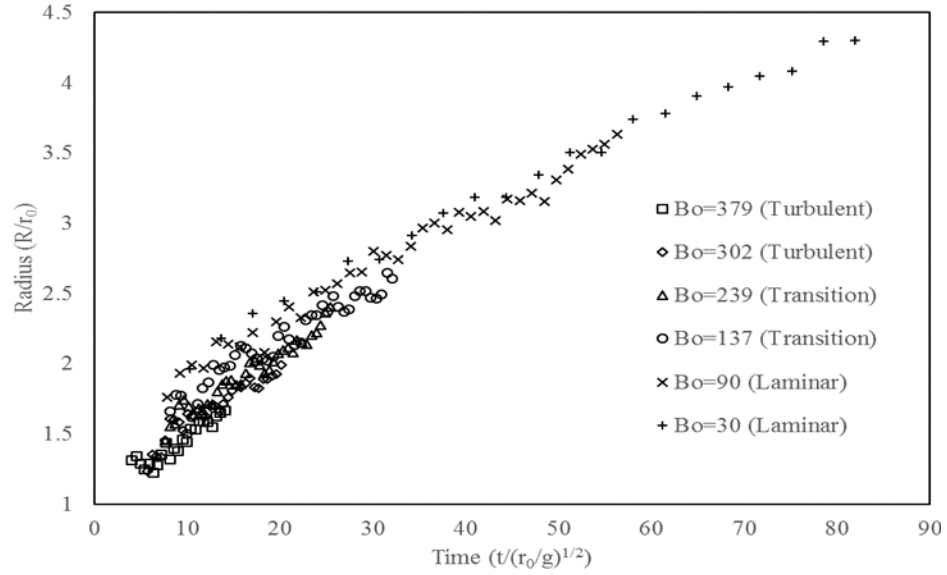
Figure 2. 9 Dimensionless radius versus dimensionless time at different Bond numbers.

2.4.2.5 Trajectory

The elevation and radius of the vortex ring have been made dimensionless using the equivalent radius r_0. The trajectory of the ring radius is roughly linear with the elevation, and at a specific elevation, the ring radius increases as Bond number decreases. As the Bond number increases, the vortex ring will form at a higher elevation.
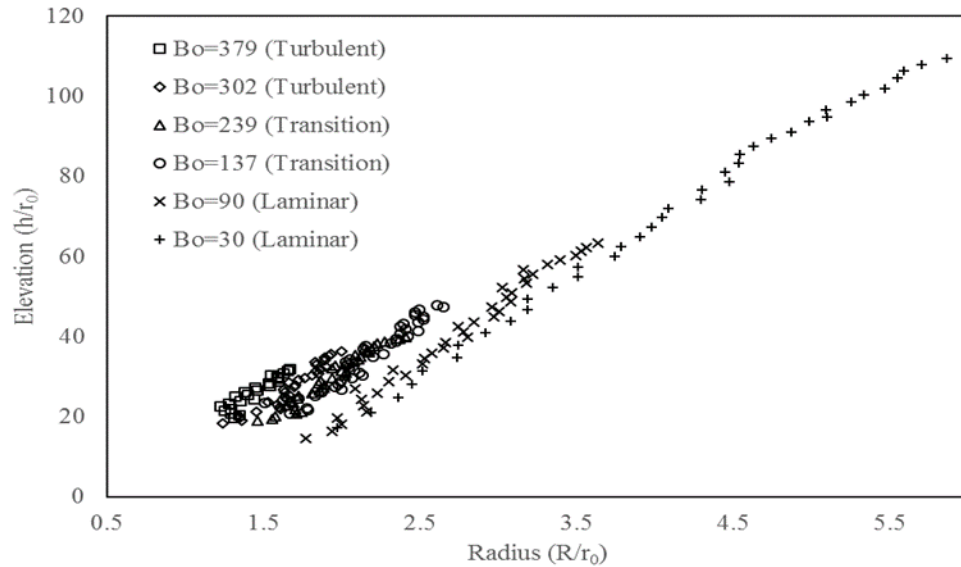
Figure 2. 10 Dimensionless elevation versus ring radius at different Bond number.

27

2.4.3 Transition Regime

2.4.3.1 Vortex Rings' Types at Different Experimental Conditions

Previous literature did not have enough discussion on the conditions under which the generator could produce a laminar buoyant vortex ring or a turbulent one. Therefore, the next section discusses the transition regime of the laminar to the turbulent vortex ring. The experiment was conducted at different air pressures for different nozzle opening times. The vortex rings at different experimental conditions are shown in Figure 2. 11.

| 180 kPa | 200 kPa | 220 kPa | 220 kPa | 240 kPa |
| 240 kPa | 260 kPa | 260 kPa | 280 kPa | 300 kPa |

(a)   Orifice D=11.1 mm (the ratio of chamber diameter to orifice diameter=3.6), ring elevation H=1.5 m, opening time t=0.1 s

| 180 kPa | 200 kPa | 200 kPa | 220 kPa | 240 kPa |

(b)   Orifice D=11.1 mm (the ratio of chamber diameter to orifice diameter=3.6), ring elevation H=1.5 m, opening time t=0.2 s
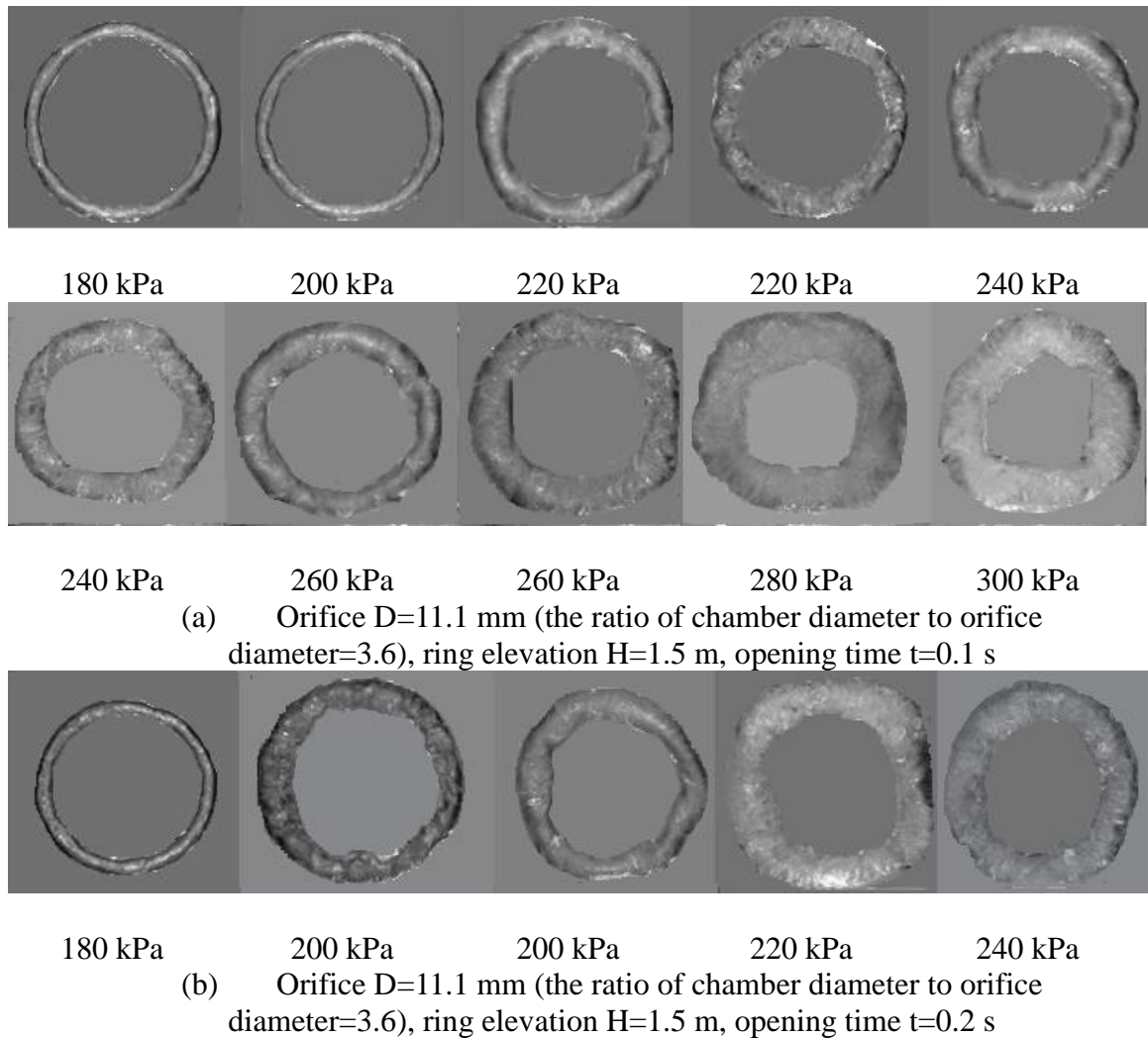
Figure 2. 11 The effect of pressure and opening time on buoyant vortex ring shape.

As seen from the figure, when the orifice opening time was 0.1 s, air pressure under 220 kPa only resulted in laminar vortex rings. When the air pressure was between 220 kPa and 260 kPa, it could sometimes produce the laminar vortex ring or the turbulent vortex rings. If the air pressure exceeded 260kPa, the experiment could only generate turbulent vortex rings. From Table 2. 2 we know that when the air pressures lower than 180 kPa, the generator will only generate cap bubbles.

When the orifice opening time was 0.2s, the air pressure at 180 kPa only generated the laminar vortex ring, while air pressure at 200 kPa could produce the laminar or turbulent vortex ring. Finally, when the air pressure was between 220 kPa and 240 kPa, it could only produce a turbulent vortex ring. It was thus anticipated that a transition regime would exist between these states laminar and turbulent conditions.

2.4.3.2 Radius Ratio

The development of the radius ratio (R/r_0) at different experimental conditions is shown in Figure 2. 12. It needs to mention that the experiment was conducted ten times at each experimental condition and the data shown here are the average value of each condition. The radius ratio increases with the elevation. It signifies that the vortex ring expands and the core radius stretches when the bubble ring rises to a higher elevation. It is easier to segregate three different regions corresponding to different vortex ring conditions in the figure. At the same elevation, the radius ratio for the laminar vortex ring is high, while the radius ratio for the turbulent vortex ring is comparatively very low. The radius ratio for the transition situation is between the laminar one and the turbulent one. Therefore, the radius ratio can be a second criterion to decide the vortex ring condition (laminar, transition or turbulent). However, the radius ratio is not a commonly used parameter to

distinguish the bubble rings' transition behavior. From Eq. (2.13), the radius ratio is the function of the Reynolds number, Bond number and Weber number. These three dimensionless numbers are commonly used in the fluid dynamics of two-phase flow. Therefore, the transition map of a buoyant vortex ring in the present study is shown in terms of these three parameters.
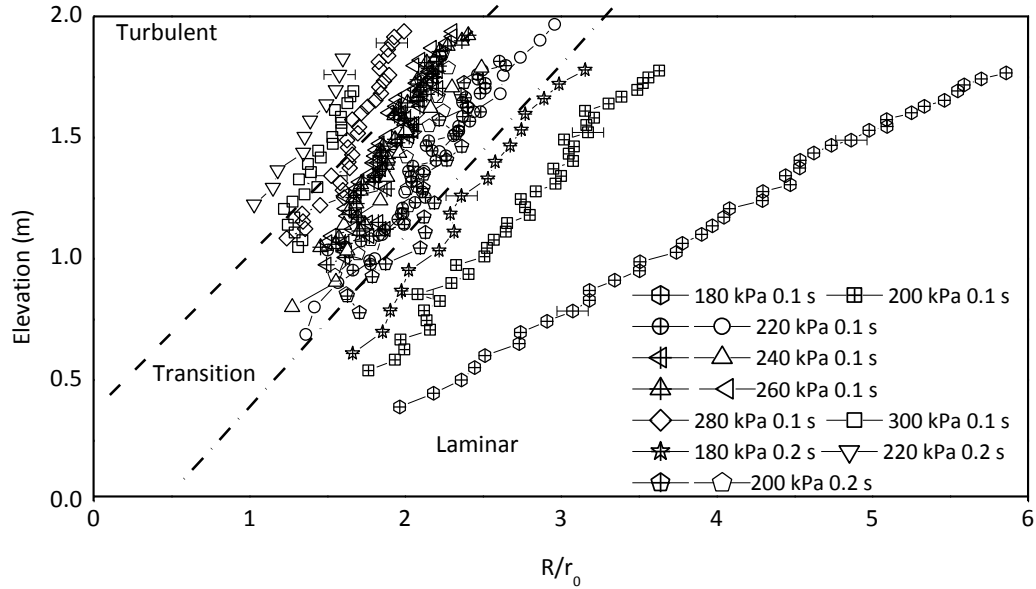
Figure 2. 12 The radius ratio development at different experimental conditions. The symbols filled with a cross signify the laminar vortex ring, while the hollow symbols represent the turbulent vortex ring.

2.4.3.3 Transition Map

As discussed before, Reynolds number, Bond number and Weber number are three key dimensionless numbers to characterize the vortex ring regime, i.e., laminar, transitional, or turbulent. The transition map is created as Reynolds number versus Bond number and Weber number. The crosses represent vortex rings that remain laminar through the observation portion of the tank (0.5 m-1.8 m above the membrane). The hollow circle represents the turbulent cases. The distinction was easily made by observing the shape of the vortex ring captured by the top camera.
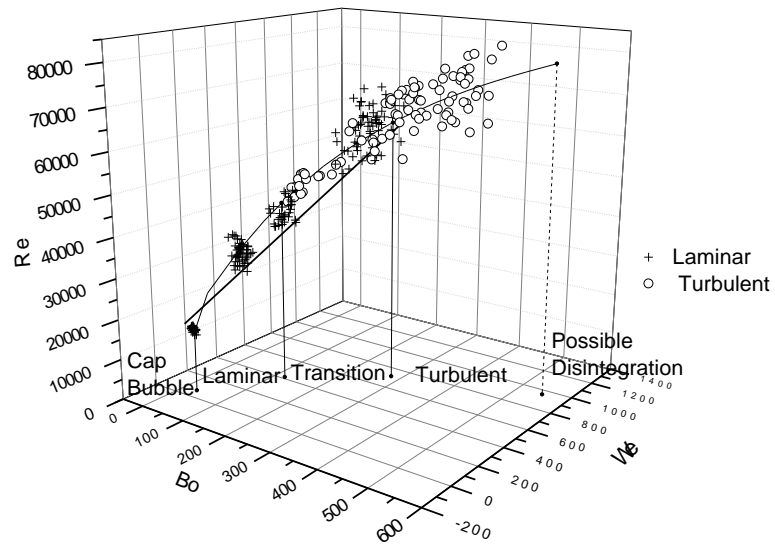
a. 3D transition map
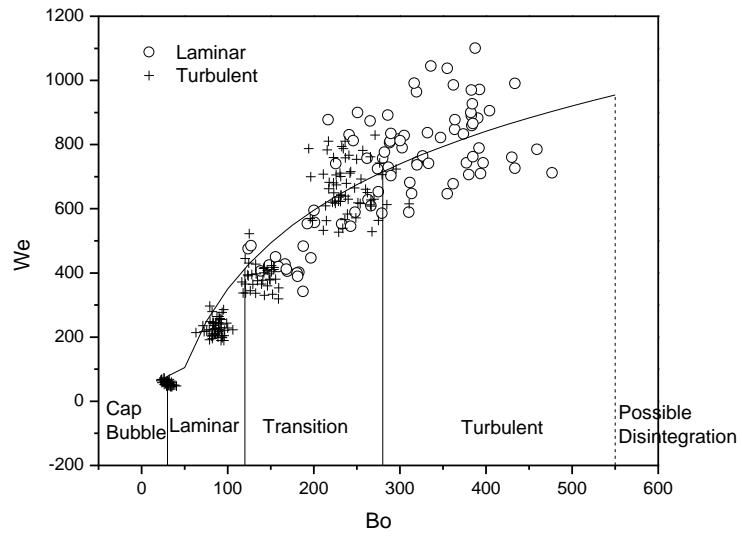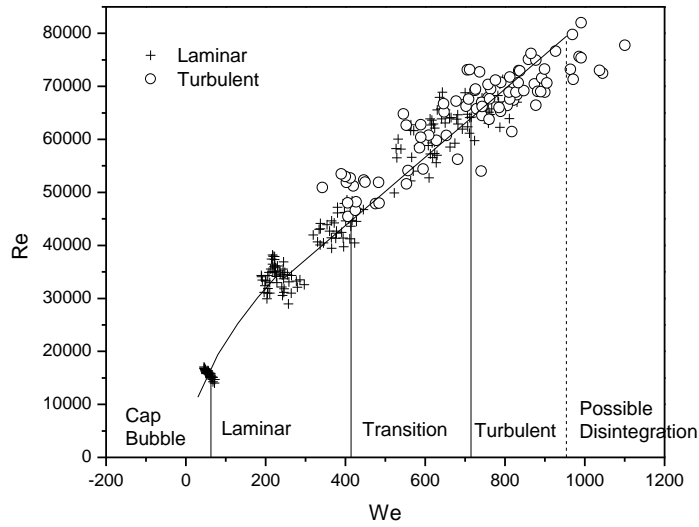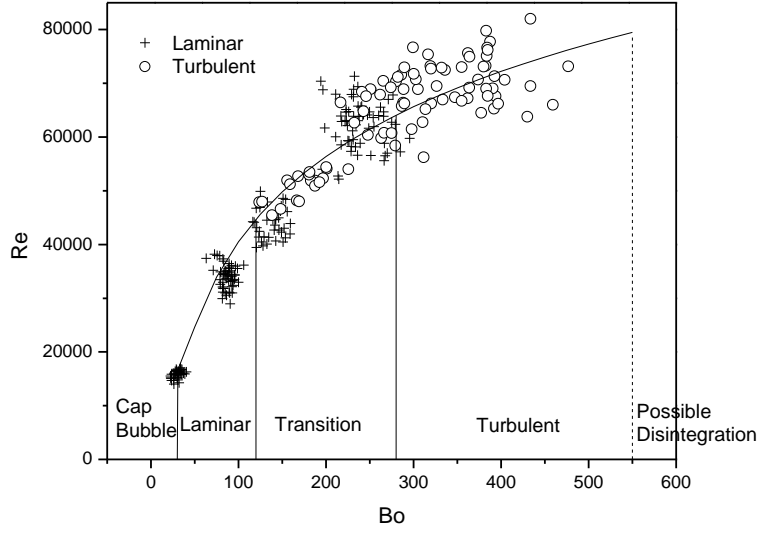
b. Side view

Figure 2. 13 Transition map of the buoyant vortex ring.

As shown in Figure 2. 13, Re=40000 to 65000, Bo=120 to 280, and We=400 to 700

delineates transitional regime for this vortex ring. For Re ≤40000, Bo≤120, We≤400, the

vortex ring was laminar. For Re≥65000, Bo≥280, We≥7000, the vortex ring was turbulent.

In addition, for Reynolds number smaller than 14000, Bond number lower than 30 and

Weber number smaller than 70, the vortex ring did not form, it will only get spherical cap bubble, as it did not have enough energy to sustain its rotation along the ring axis.

In theory, when the azimuthal wave amplitude is too high, the vortex ring may not be able to sustain such large disturbances and it should break into collapse bubbles. In addition, as Weber number increases, the inertia of the vortex ring will also increase and suppress the action of the surface tension. Then the area of the vortex ring will continuously increase, which will finally lead the vortex ring into collapse bubbles. There should be an upper limit beyond which the ring cannot be produced. Due to limitations of our equipment, we could not investigate that upper limit.

2.4.3.4 Comparison with Other Studies

From the data provided by Vasel et al. [28], and Lundgren and Mansour [29], we can calculate their Weber number, Bond number, and Reynolds number. Their data are plotted in Figure 2. 13. It can be seen that their results almost coincide with our trend. The deviation is likely due to the different vortex ring generation system. Vasel et al. generated the vortex ring by using a pin to puncture the balloons. The initial velocity of his vortex ring was zero. While the vortex ring in this paper has initial velocity owing to the compressed air pressure. Thus, the inertia of the vortex ring will be different even at the same Bond number. Therefore, the Reynolds number and Weber number will have some deviation. In general, the data almost follows the trend.

2.5 Conclusion

Formation and evolution characteristics of a buoyant vortex ring were investigated experimentally using with different orifice diameters, orifice opening times, and air pressures. The ratio of the chamber diameter to orifice diameter can influence the formation

potential and working pressure range of the vortex ring. When it is too small or too big, formation potential is reduced. The suitable ratio is around 3.6 to 4.2. In addition, previous experimental investigations of the bubble ring did not provide the information on the relationship between a certain formation conditions and the formation of a particular kind of the bubble ring. In this paper, we characterize the formation conditions of a buoyant vortex ring, its transition behavior from a laminar to a turbulent vortex ring, and its disintegration. For Reynolds numbers between 40000 and 65000, Bond numbers between 120 and 280, and Weber numbers between 400 and 700 delineate a zone of laminar to turbulent regime transition. Below this, we were only able to produce laminar vortex rings, and above this we could only get turbulent vortex rings. For Reynolds numbers lower than 14000, Bond numbers lower than 30, and Weber numbers smaller than 70, we were not able to generate vortex rings. Moreover, some basic flow parameters of a bubble ring have been studied. The rising velocity, radius, and trajectory of a buoyant vortex ring is changed by the Bond number.

Acknowledgment

References

[1] O.V. Fuentes, Early observations and experiments on ring vortices, Eur. J. Mech. B/Fluids 43 (2014) 166-171.

[2] H. Lamb, Hydrodynamics, Cambridge University Press, Cambridge, 1932.

[3] D.S. Chapman, P.R. Critchlow, Formation of vortex rings from falling drops, J. Fluid Mech. 29 (1967) 177-185.

[4] T. Maxworthy, The structure and stability of vortex rings, J. Fluid Mech. 51 (1972) 15.

[5] N. Didden, On the formation of vortex rings: rolling-up and production of circulation, J. Appl. Math. Phys. 30 (1) (1979) 101-116.

[6] K. Shariff, A. Leonard, Vortex rings, Annu. Rev. Fluid Mech. 24 (1992) 235-279.

[7] T.T. Lim, T.B. Nickels, Vortex rings, in: Green S.I. (Ed.), Fluid Vortices, Springer, Netherlands, 1995, pp. 95-153.

[8] M. Gharib, E. Rambod, K. Shariff, A universal time scale for vortex ring formation, J. Fluid Mech. 360 (1998) 121-140.

[9] H. Tang, S. Zhong, M. Jabbal, et al., Towards the design of synthetic-jet actuators for full-scale flight conditions, Flow Turbul. Combust. 78 (2007) 309-329.

[10] M. Rosenfeld, K. Katija, J.O. Dabiri, Circulation generation, and vortex ring formation by conic nozzles, J. Fluids Eng. 131 (9) (2009) 091204.
[11] J.O. Dabiri, Optimal vortex formation as a unifying principle in biological propulsion, Annu. Rev. Fluid Mech. 41 (1) (2009) 17-33.

[12] M. Krieg, K. Mohseni, Modelling circulation, impulse, and kinetic energy of starting jets with non-zero radial velocity, J. Fluid Mech. 719 (2013) 488-526.

[13] N. Takagaki, R. Kurose, Y. Baba, et al., Relationship between the momentum of an impinging drop and intensities of vortex rings generated below free surface, Int. J. Multiph. Flow 65 (2014) 1-10.

[14] A. Weigand, M. Gharib, On the evolution of laminar vortex rings, Exp. Fluids, 22 (6) (1997) 447-457.

[15] P.F. Linden, The interaction of a vortex ring with a sharp density interface: a model for turbulent entrainment, J. Fluid Mech. 60 (3) (1973) 467-480.

[16] A. Glezer, The formation of vortex rings, Phys. Fluids, 31 (1988) 3532-3542.

[17] K. Bourne, S. Wahono, A. Ooi, Numerical investigation of vortex ring ground plane interactions, J. Fluids Eng. 139 (7) (2017) 071105.

[18] A. Weigand, M. Gharib, Turbulent vortex ring/free-surface interaction, J. Fluids Eng. 117 (1995) 374-381.

[19] A. Falahatpisheh, A. Kheradvar, A measure of axisymmetry for vortex rings, Eur. J. Mech. B/Fluids 49 (2015) 264-271.

[20] M. Cheng, J. Lou, T.T. Lim, Evolution of an elliptic vortex ring in a viscous fluid, Phys. Fluids 28 (2016) 037104.

[21] B. Chen, Z. Wang, G. Li, Y. Wang, Experimental investigation of the evolution and head-on collision of elliptic vortex rings, J. Fluids Eng. 138 (3) (2016) 031203.

[22] J.K. Walters, J.F. Davidson, The initial motion of a gas bubble formed in an inviscid liquid, J. Fluid Mech. 17 (1963) 321-336.

[23] J.S. Turner, Buoyant vortex rings, Proc. Roy. Soc. Lond. A: Math. Phys. Eng. Sci. 239 (1957) 61-75.

[24] T.J. Pedley, The toroidal bubble, J. Fluid Mech. 32 (1968) 97-112.

[25] M. Shusser, M. Gharib, A model for vortex ring formation in a starting buoyant plume, J. Fluid Mech. 416 (2000) 173-185.

[26] T.S. Pottebaum, M. Gharib, The pinch-off process in a starting buoyant plume, Exp. Fluids 37 (2004) 87-94.
[27] D. Bond, H. Johari, The impact of buoyancy on vortex ring development in the near field, Exp. Fluids 48 (2009), 737-745.

[28] A.R. Vasel-Be-Hagh, R. Carriveau, D.S.-K Ting, A balloon bursting underwater, J. Fluid Mech. 769 (2015) 522-540.

[29] T.S. Lundgren, N.N. Mansour, Vortex ring bubbles, J. Fluid Mech. 224 (1991) 177-196.

[30] R.P. Satti, A.K. Agrawal, Computational study of buoyancy effects in a laminar starting jet, Int. J. Heat Fluid Flow 29 (2008) 527-539.

[31] L. Gao, S.C.M. Yu, A model for the pinch-off process of the leading vortex ring in a starting jet, J. Fluid Mech. 656 (2010) 205-222.

[32] R. Ganapathy, Weak thermal vortex rings, J. Fluids Eng. 116 (1) (1994) 174-176.

[33] S.S.H. Chang, Motion of a large dusty buoyant thermal with a vortex ring, J. of Appl. Mech. 45 (4) (1978) 711-716.

[34] C. Solomon, T. Breckon, Fundamentals of Digital Image Processing: A practical approach with examples in Matlab, John Wiley & Sons, 2011.

CHAPTER 3 NATURAL TRANSPORTATION: BUOYANT VORTEX RINGS

3.1 Introduction

A vortex ring can be characterized as either a buoyant or non-buoyant vortex ring depending on whether the fluid density is lighter than the ambient fluid or not. Unlike non-buoyant (homogeneous) vortex rings, which have been studied extensively for over a century, both numerically [1, 2] and experimentally [3, 4], the study of buoyant vortex rings started relatively late. Buoyant vortex rings are often observed when some marine animals, such as dolphins or whales, breathe. Some swimmers can also produce buoyant vortex rings underwater with practice. In engineering, some people have suggested that buoyant vortex rings can be a natural transportation medium to transport energy and seeding materials efficiently. Thus, it is of interest to examine the properties of a buoyant vortex ring.

Past studies on buoyant vortex rings have focused on theoretical analysis [5, 6] along with some experimental explorations [7, 8]. These studies mainly focus on the formation, lifetime, and pinch-off progress of a buoyant vortex ring and provide valuable insights into the characteristics of buoyant vortex rings. However, many unknowns remain. For example, the energy development of a vortex ring bubble has not yet been reported.

The present paper reports the propagation dynamics of a buoyant vortex ring studied experimentally. The vortex ring bubble was generated by releasing a small amount of compressed air from the bottom of a water tank. The air volume was changed by setting the compressed air at different operating pressures. The experimental investigation was applied to the idea of using the vortex ring to transport energy.

3.2 Vortex Rings

3.2.1 Vortex Ring Parameters
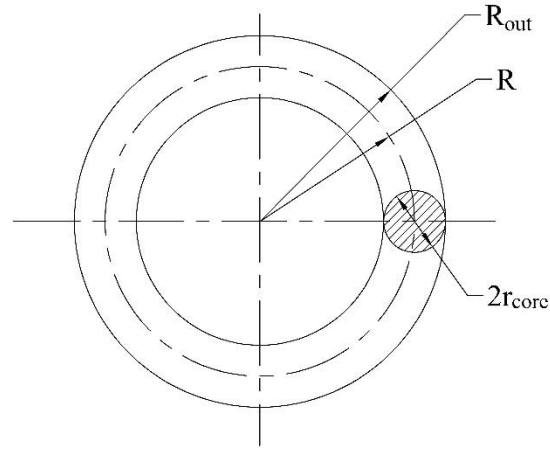
Figure 3. 1 Vortex ring parameters

The basic vortex ring parameters are shown in Figure 3. 1. R_{outer} is the outer radius of

the vortex ring, R is the ring radius, and r_{core} is the vortex core radius. The structure of the

vorticity in the core of the vortex ring can categorize the vortex ring into either a thin core

ring or a thick core ring. If the vorticity is confined to a small region compared to the ring

diameter, it is a thin core vortex ring. If the vorticity spreads to cover the moving region, it

is a thick core ring. The difference in vorticity distribution leads to different energy and

velocity of a vortex ring. If the relative core size (r_{core}/R) is smaller than $\sqrt{2}$, then the vortex

ring is a thin core structure; otherwise, it is a thick core ring [9]. The ring currently under

study is of thin core structure (Chapter 3.4.3).

3.2.2 Model

The model for a thin core structure vortex ring is developed by Sullivan et al. [10].

The rising velocity and the kinetic energy for a thin core vortex ring is

$$V = \frac{\Gamma}{4\pi R}\left(\ln\left(\frac{8R}{r_{core}}\right) - \frac{1}{4}\right) \tag{3.1}$$

$$E_k = \frac{1}{2}\rho\Gamma^2 R\left(\ln\left(\frac{8R}{r_{core}}\right) - \frac{7}{4}\right) \tag{3.2}$$

where Γ is the circulation of a buoyant vortex ring and ρ is the ambient fluid density. The rising velocity, ring radius and core radius are the parameters that can be directly obtained from the experimental video. From Eq. (3.1), the circulation of the vortex ring can be deduced as

$$\Gamma = 4\pi RV / (\ln(\frac{8R}{r_{core}} - \frac{1}{4}) \tag{3.3}$$

3.2.3 The Mechanical Energy of a Buoyant Vortex Ring

The mechanical energy of a buoyant vortex ring is the expression of its own kinetic energy (E_k) and potential energy

$$E = E_k + E_p \tag{3.4}$$

Potential energy equals the negative of the work done by the conservative force. For most of the occasions in the present study, the vortex ring is fully formed at a height around 1 m above the membrane. Therefore, we set the potential energy at an elevation equal to 1 m as zero. For an object submerged underwater, the potential energy consists of buoyant potential energy E_{pb} and gravitational potential energy E_{pg}. The gravitational potential energy is generated by gravity. It increases as the ring rises. The gravitational potential energy of a bubble ring at elevation z_i is

$$E_{pg} = \int_1^{z_i} \rho_a g \Omega_z dz \tag{3.5}$$

where Ω_z is the volume of the buoyant vortex ring at z and ρ_a is the air density. When the vortex ring is underwater, there is a strong buoyant force acting on it. The buoyancy force is also a conservative force, creating a "buoyant potential energy" (analogous to gravitational potential energy, but due to the buoyant force and not gravity). As the bubble

rises, the buoyant force exerts positive work on the bubble ring, leading to a decrease in buoyant potential energy. So the buoyant potential energy at elevation z_i can be expressed as

$$E_{pb} = -\int_1^{z_i} \rho_w g \Omega_z dz \tag{3.6}$$

where ρ_w is the water density.

The kinetic energy E_k of a vortex ring is the sum of the traveling kinetic energy and the energy related to the rotating core. It can be calculated by Eq. (3.2). The total potential energy of a buoyant vortex ring is

$$E_p = E_{pb} + E_{pg} = -\int_1^{z_i}(\rho_w - \rho_a)g \Omega_z dz \tag{3.7}$$

As the bubble ring rises, the pressure on it decreases, leading to a change in the ring volume. Applying the ideal gas equation over the range of traversed elevation, considering a constant air temperature, then the ring volume at elevation z is

$$\Omega_z = \frac{P_0 \Omega_0}{P_z} \tag{3.8}$$

where P_0, Ω_0 and P_z are the surrounding pressure of initial fully formed vortex ring ($z = z_0$), the volume of the initial buoyant vortex ring and the surrounding pressure at elevation z. Considering that $P = \rho g h$, Eq. (3.8) can be written as

$$\Omega_z = \frac{(h_{amb} + H - z_0)\Omega_0}{(h_{amb} + H - z)} = (1 + \frac{z - z_0}{(h_{amb} + H - z)})\Omega_0 \tag{3.9}$$

h_{amb} is the atmospheric pressure in meters of water (10.3 m), and H is the water height above the membrane (H=1.8 m), (H-z) represents the depth of the buoyant vortex ring.

Substituting Eq. (3.9) into Eq. (3.7), we obtain

$$E_p = (\rho_w - \rho_a)g(h_{amb} + H - z_0)\Omega_0(\ln(h_{amb} + H - z) - \ln(h_{amb} + H - 1)) \tag{3.10}$$

Note ln (h_{amb}+H-1)$\approx$2.4. By combining Eq. (3.2) and Eq. (3.8), the mechanical energy of a buoyant vortex ring can be written as

$$E = (\rho_w - \rho_a)g(12.1 - z_0)\Omega_0(\ln(12.1 - z) - 2.4) + \frac{1}{2}\rho_w \Gamma^2 R(\ln\left(\frac{8R}{r_{core}}\right) - \frac{7}{4}) \tag{3.11}$$

3.3 Experiment Setup

The experiments were conducted in a Plexiglas tank with dimensions of 0.8 m × 0.8 m × 2.4 m high. The experiment setup is shown in Figure 3. 2. The tank was filled with water up to 1.8 m above the opening membrane of the vortex generation chamber. Compressed air moved through a pressure regulator to a solenoid valve controlled by a programmable logic controller (PLC). When the solenoid valve opened, the air pushed the piston up against the force of the spring. Once the piston was lifted, compressed air rushed into the vortex generation chamber and burst out through the small nozzle on a flexible membrane. The membrane is made of aluminum with a thickness of 0.072 mm (0.003 inches).

All the experimental data were obtained photographically by a two-camera image acquisition system. This system consisted of two cameras perpendicular to each other. One was positioned on the top of the tank; the resolution of this camera was 1920×1080 with a speed of 30 fps; another camera was in front of the tank at a resolution of 1280×720 with a speed of 120 fps. This experiment also used two auxiliary backlights on the side and top respectively to outline the vortex ring clearly.

The recorded videos were then analyzed frame-by-frame using the Matlab program to deduce the dimensions and propagation rate of the vortex ring. The spreading rate ($\alpha=dR/dz$) and rising velocity ($V=dz/dt$) can be determined as $\Delta R/\Delta z$ and $\Delta z/\Delta t$.
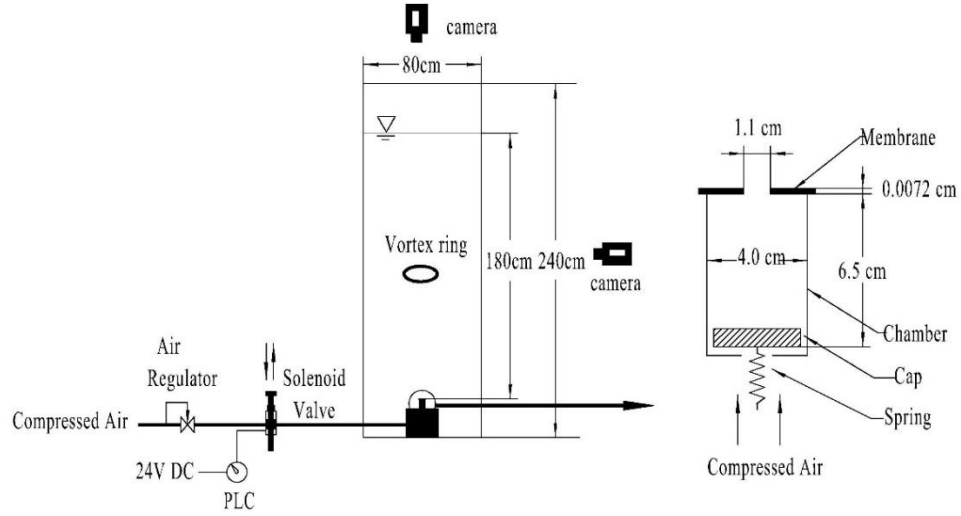
Figure 3. 2 Experimental apparatus.

The Bond number is a ratio of the body force to the surface tension. A high value of the Bond number indicates that the system is relatively unaffected by surface tension effects. The Bond number is usually used to characterize the shape of the bubbles moving in a surrounding fluid. When using the vortex ring method to transport the materials, a higher Bond number means the ring has a higher body force if the surface tension is constant. In other words, the vortex ring can sustain more materials (larger volume of the vortex ring). It is important to study the flow behavior of the bubble ring at different Bond numbers (comparing different vortex ring sizes against corresponding vortex ring characteristics). As a result, this paper used the Bond number to characterize the vortex ring, given as

$$Bo = \frac{\rho g r_0^2}{\sigma} \tag{3.12}$$

where r_0 is the equivalent spherical radius of a vortex ring, σ is the surface tension of the air-water system. The surface tension of an air-water system at 20 °C is $\sigma=72.8\times10^{-3}$ N/m. The Bond number in the current study can be controlled by the inlet air pressure and the duration of release time. The compressed air at 180 kPa, 220 kPa, 260 kPa and 300 kPa over a duration of 0.1 s was released in the present study, leading to the examined Bond

number values were 30±8, 137±15, 239±13, and 379±17 with a confidence level of 95%.

3.4 Results and Discussion

3.4.1 Rising Velocity
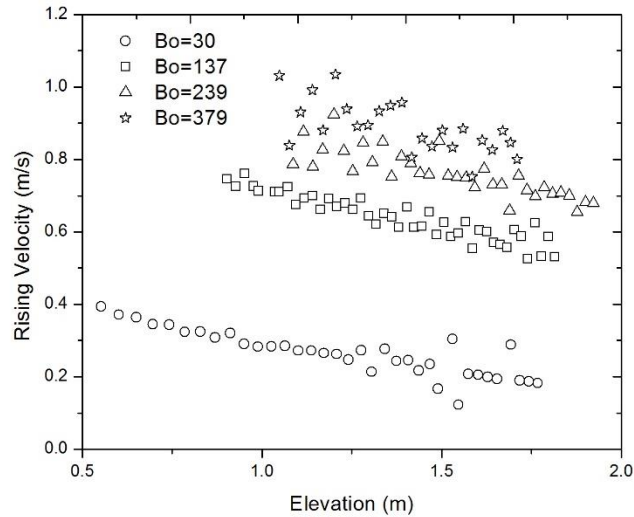
Figure 3. 3 Rising velocity versus elevation.

Study of the rising velocity of a buoyant vortex ring can provide some insight on the travel behavior of a buoyant vortex ring. Figure 3. 3 is a plot of vortex rings' rising velocity with elevation as they rise. As is observed, the rising velocity decreases with elevation (time) at a fixed Bond number. The velocity decrease may be because when the vortex ring forms, an azimuthal wave will grow on the perimeter of the ring. This azimuthal wave extracts the energy from the vortex ring, slowing its motion. When the velocity becomes very slow, the viscous force will become dominant and stop the ring from rising. As a result, the vortex ring should have a finite lifetime.

It can also be observed that the rising velocity increases as the Bond number increases. A higher Bond number means the vortex ring has higher initial kinetic and potential energy,

resulting in a larger rising velocity. As the initial amount of energy increases, the initial velocity of a bubble ring also increases so that it can travel further and have a longer lifetime. The buoyant vortex ring decelerates as it rises. If we need to use the vortex ring for transportation, we need to supply enough energy to prevent it from breaking up before reaching our desired distance.

Furthermore, the velocity fluctuates more as the Bond number increases. The azimuthal wave breaks the stability of a vortex ring and bends the ring into the wavy unstable stage. The wave disturbance becomes stronger as the Bond number increases.

3.4.2 Ring Radius
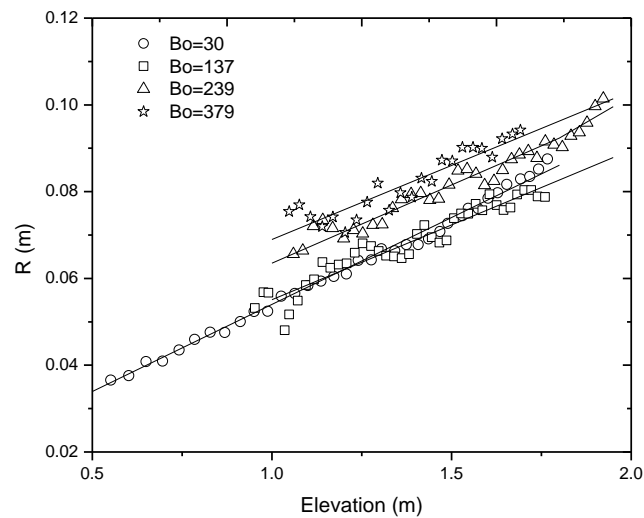
Figure 3. 4 Ring radius versus elevation.

The development of the vortex ring radius is shown in Figure 3. 4. The vortex ring expands as it rises. The ring size grows linearly as the bubble rises. In addition, the higher Bond number has a larger ring radius. It can also be observed that the initial vortex ring forms at a higher elevation as Bond number increase.

3.4.3 Relative Core Size

The evolution of the relative core size r_{core}/R is shown in Figure 3. 5. The core structure stretches as it rises. The ring radius expands and the volume of the buoyant vortex ring is almost constant. As a result, the core size decreases. In the present study, the volume change is around 8%. The small deviation of the volume is due to pressure change with elevation.

From the beginning of a buoyant vortex ring to its development, the relative core radius r_{core}/R is always smaller than $\sqrt{2}$. This illustrates that the buoyant vortex ring is a thin core structure [9]. Thus, the vorticity in the center of a thin core ring is almost zero due to its distance from the vorticity structure of the ring. This allows the circulation of the buoyant vortex ring to remain almost constant (discussed later).
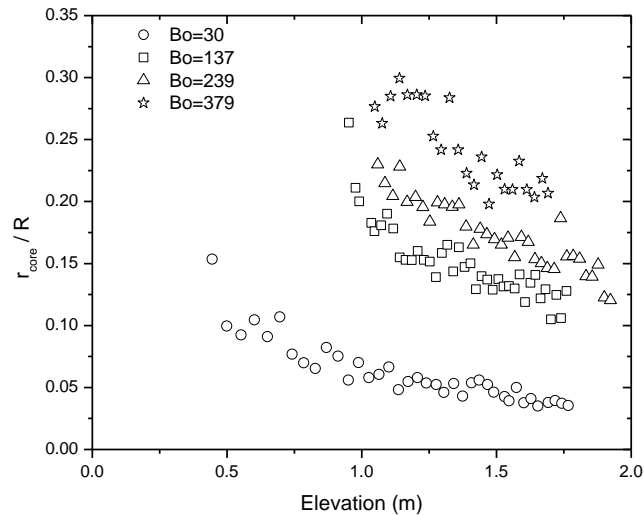
Figure 3. 5 Relative core size versus elevation

3.4.4 Circulation

The development of the circulation of the vortex ring is shown in Figure 3. 6. Under special operating conditions, the circulation remains almost constant as the ring rises. The

maximum standard deviation of the circulation is approximately 10%. This suggests that the vorticity is only confined near the core structure. It does not lose to the wake and extends to the symmetry axis. The buoyant vortex ring can prevent the seeding material (the vortex ring fluid) in the core from spreading over the moving region.

It can also be observed that the circulation increases as the Bond number increases. Sullivan et al. [10] found that the circulation increases with the piston speed, which means higher kinetic energy could cause an increase in the circulation. Vasel et al. [11] used the balloon rupture method to generate the buoyant vortex ring. The initial velocity of the ring bubble is zero. He concluded that the circulation increases with the balloon size. Higher potential energy results in higher circulation. In the current study, the higher operating compressed air pressure leads to both higher initial potential energy and initial kinetic energy. This higher potential energy and kinetic energy work together to increase the circulation of the buoyant vortex ring. Therefore, the rise in circulation is not related to the form of the energy but the amount of initial energy.
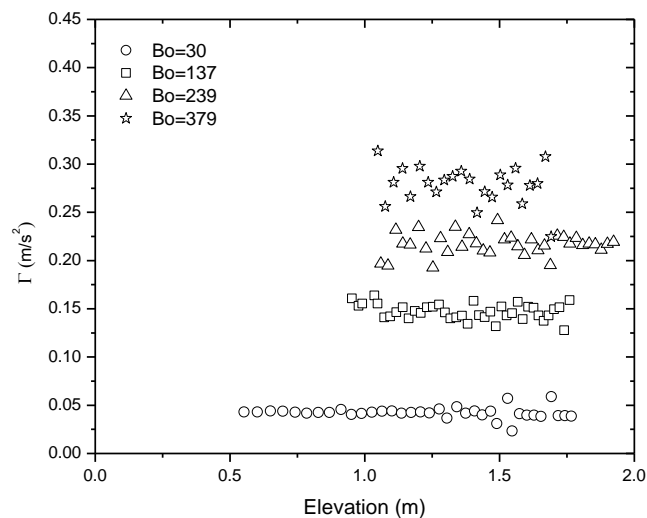
Figure 3. 6 Circulation versus elevation.

3.4.5 Energy

Figure 3. 7 compares the mechanical energy with different Bond numbers. The buoyant vortex ring with the higher Bond number has higher mechanical energy. This is because the higher Bond number vortex ring in the current study has higher initial kinetic energy and potential energy. If we want the vortex ring to move a longer distance, we can increase the initial energy given to the vortex ring.
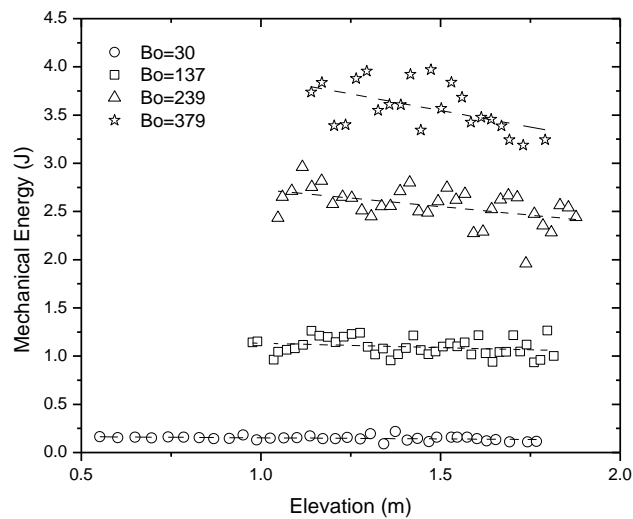
Figure 3. 7 Mechanical energy of a buoyant vortex ring versus elevation.

In addition, the mechanical energy slightly decreases as the bubble rises. The energy decay trend is more obvious as the Bond number increases. As mentioned before, an azimuthal disturbance grows with the vortex ring as it proceeds. This bending wave can extract the energy from the vortex ring [12]. The wave disturbance of the vortex ring with a lower Bond number is small so that the energy loss is minimal compared to the one with the higher Bond number. In terms of energy loss, it is better to generate a small Bond number vortex ring to transfer the materials.

Figure 3. 8 shows the kinetic energy of a buoyant vortex ring. The kinetic energy of

the vortex ring increases as it travels up. It is mainly because of the decrease of the potential energy. Moreover, a vortex ring with higher vorticity (larger circulation) has much more kinetic energy. In nature, the buoyancy force propels the buoyant vortex ring to travel. Because of the lower mechanical energy loss and the natural propulsion of the buoyancy force, the buoyant vortex ring can move a long distance.
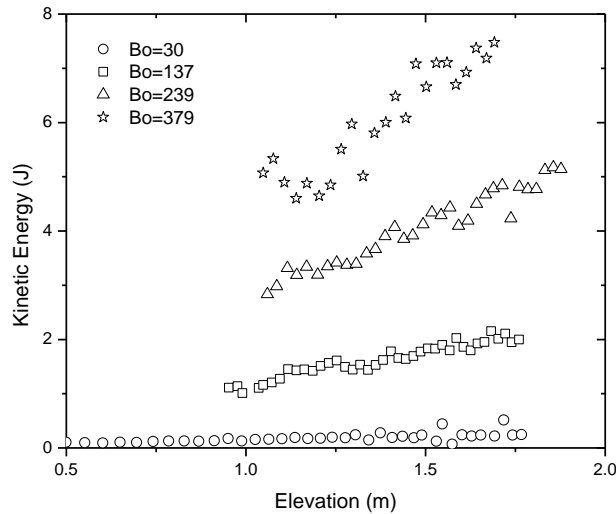
Figure 3. 8 Kinetic energy of a buoyant vortex ring versus elevation.

3.5 Conclusion

The buoyant vortex ring is a thin core structure. A thin core structure guarantees that the circulation of a buoyant vortex ring remains almost constant so that the elements forming a buoyant vortex ring does not lose to the wake. As buoyant vortex rings rise, they expand, their rising velocity decreases, while the core stretches. The higher the amount of energy given to a vortex ring, the more circulation a vortex ring will attain. The increase in circulation (vortex strength) leads to the vortex ring traveling faster and longer distances. However, the influence of the azimuthal disturbance around vortex rings is greater for rings with higher circulation, diffusing more energy to the surrounding area. Thus, when using a

48

vortex ring to travel the desired distance with a minimal energy loss, it is better to give sufficient energy to the vortex ring to sustain its ring structure; extra energy will lead to a higher dissipation of the energy.

Acknowledgements

References

[1] K. Mohseni, H. Ran, T. Colonius, Numerical experiments on vortex ring formation, J. Fluid Mech. 430 (2001) 267-282.

[2] M. Rosenfeld, K. Katija, J.O. Dabiri, Circulation generation and vortex ring formation by conic nozzles, J. Fluids Eng. 131(9) (2009) 091204.

[3] T. Maxworthy, The structure and stability of vortex rings, J. Fluid Mech. 51(01) (1972) 15-32.

[4] N. Didden, On the formation of vortex rings: rolling-up and production of circulation, Z. Angew. Math. Phys. 30(1) (1979) 101-116.

[5] L. Gao, S.C.M. Yu, A model for the pinch-off process of the leading vortex ring in a starting jet, J. Fluid Mech. 656 (2010) 205-222.

[6] J. Lou, M. Cheng, T.T. Lim, Evolution of an elliptic vortex ring in a viscous fluid, Phys. Fluids 28 (2016) 037104.

[7] J.S. Turner, Buoyant vortex rings, Proc. R. Soc. Lond. A Math. Phys. Sci. 239 (1957) 61-75.

[8] A. Vasel-Be-Hagh, R. Carriveau, D.S.K. Ting, J.S. Turner, Drag of buoyant vortex rings, Phys. Rev. E 92(4) (2015) 043024.

[9] L.E. Fraenkel, Examples of steady vortex rings of small cross-section in an ideal fluid. J. Fluid Mech. 51 (1972) 119-135.

[10] I.S. Sullivan, J.J. Niemela, R.E. Hershberger, D. Bolster, R.J. Donnelly, Dynamics of thin vortex rings, J. Fluid Mech. 609 (2008) 319-347.

[11] A. Vasel-Be-Hagh, R. Carriveau, D.S.K. Ting, A balloon bursting underwater, J. Fluid

Mech. 769 (2015) 522-540.

[12] R.E. Hershberger, D. Bolster, R.J. Donnelly, Slowing of vortex rings by development of kelvin waves, Phys. Rev. E 82(3) (2010) 036309.

CHAPTER 4 VORTICAL FLOW STRUCTURES BEHIND A TORUS WITH AN

ASPECT RATIO OF THREE

4.1 Introduction
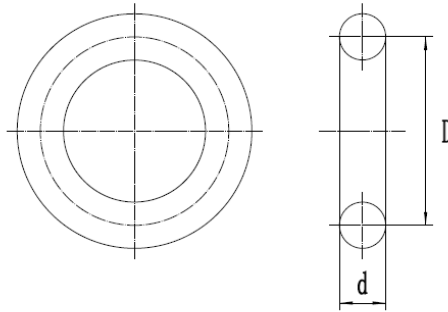
Figure 4. 1 Parameters of the torus.
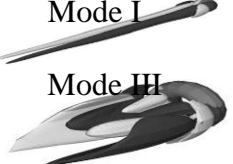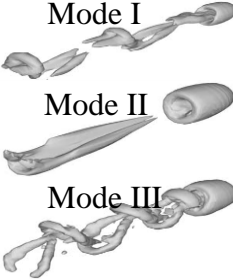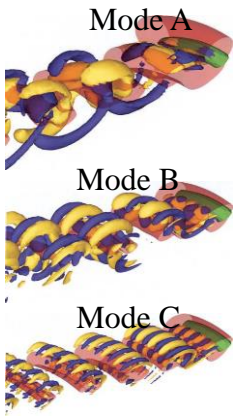
The flow that passes a torus has become a popular focus of study due to its special

geometry. The shape of the torus is characterized by the aspect ratio Ar = D/d, where d is

the cross-section diameter and D is the mean diameter (Figure 4. 1). As such, the point

where the aspect ratio equals zero represents a sphere, while it denotes a circular cylinder

when it approaches infinity [1]. The difference in the wake structure between the sphere [2]

and cylinder [3, 4] motivates people to study the geometric effect on the flow across the

bluff body. In practice, investigations of the flow structure of the torus have contributed to

improved understanding in bio-fluid mechanics for DNA polymers [5], flow problems with

micelles [6], and the drag and heat transfer of helical heating tubes [7].

Roshko [8] conducted one of the earliest studies on the flow over a torus and found

that the vortex shedding of a torus with Ar = 10 is almost the same as those shed from a

circular cylinder. He also found a decrease in the shedding frequency between the bluff

rings and from that of a circular cylinder. This seminal study spurred many others

investigate flow past the torus. The flow pattern downstream of a torus of different aspect ratios is summarized in Table 4. 1. To highlight, Inoue et al. [9] used an Ultrasound Doppler Velocity Profiling (UVP) monitor to study the vortex shedding of the torus (Ar = 3 and 5) at a Reynolds number of 1500. They monitored the distinct wake structure for these two tori. Wang et al. [10] simulated flow past a torus with Ar = 0.5 and 2 by comparing the results with sphere wake structures and found them to be very similar. As seen in Table 4. 1, the wake structure of a torus with Ar< 3.9 is analogous to a sphere wake structure; in particular, the aspect ratio Ar< 1.6 has the same transition behavior as the sphere. The flow pattern of Ar>3.9 is similar to a circular cylinder. The shedding frequency and the wake structure behind a torus with an Ar>3.9 have been investigated extensively, both numerically and experimentally. Studying the torus has shed light on the very different wake behavior of the sphere from that of the straight circular cylinder.

Partly because the flow pattern downstream of a torus with Ar<3.9 is asymmetric, accurate simulation of the shedding frequency can be quite challenging, and thus, rarely attempted. The few attempts [1, 20] are confined to small Reynolds numbers (Re<400). The experiments of Monson [14] involved observing a ring falling through a liquid, making Strouhal-number measurements difficult. Inoue et al. [9] only obtained the shedding frequency associated with a torus of Ar = 3 and 5 at a Reynolds number of 1500. There is a gap in our understanding of the wake structure, especially concerning the vortex shedding frequency of a torus with 1.6<Ar<3.9 at Reynolds numbers larger than 1500. In the current study, a torus with an aspect ratio of three is experimentally investigated. This paper studied the flow downstream of a torus in the wind tunnel at Reynolds numbers of 9×10^3, 1.2×10^4 and 1.5×10^4.

Table 4. 1 The wake structure behind a torus with $0 \leq Ar \leq \infty$.

Ar	Re	Flow pattern	Wake Structure	St	Flow characteristic
0~3.9	~80	Steady flow	-	-	Yu [11]
	80~90<Re< 140~275	Ar=0~1.6: Steady asymmetric Mode I Ar=1.6~1.8: A Hopf unsteady transition Mode II Ar=1.8~3.9: Steady asymmetric Mode III (Sheard et al. [1, 12, 13])	Mode I Mode III	The St for small aspect ratios is smaller than that of a circular cylinder [8, 14].	The wake structure is analogous to a sphere or disk wake structure [14, 15]. The sphere-type hairpin wake structure (oblique vortex loops) can be observed [1].
	Re>140~275	Ar=0~1.6: Mode I → Hopf bifurcation (regular asymmetric transition mode of sphere) Ar=1.6~1.8: Mode II Ar=1.8~3.9: Mode III → Hopf bifurcation (a regular asymmetric transition) (Sheard et al. [1, 12, 13])	Mode I Mode II Mode III		
3.9~∞	~50	Steady Flow	-	-	-
	Re>50	The wake at first is axisymmetric annular vortex street (ring-type structure). Three different asymmetric instabilities will apply to the axisymmetric ring-type structure as Reynolds number increases [1, 12, 13]. The sequence of each instability on the wake structure is different with the aspect ratios: Ar=3.9~8: C-A-B Ar=8~13: A-C-B Ar=13~∞: A-B-C	Mode A Mode B Mode C	$S(Re, Ar, \theta)= \{S(Re, Ar = \infty)- 0.0004268/Ar\times [Re-Re_c(Ar = \infty)]\} \times\cos\theta$ θ is the angle of vortex street being shed with respect to the torus axis (Leweke and Provansal [16])	The wake structure is axisymmetric vortex sheets, similar to the circular cylinder without end effects [14-16].

[a] The span wise wavelength of Mode A, Mode B and Mode C instability is different ($\lambda_A \approx 4d$, $\lambda_B \approx 1.7d$ and $\lambda_C \approx 0.8d$). Mode A and Mode B are analogous to the instabilities of a circular cylinder [17, 18]. Mode C is the instability for a square cylinder [19]

4.2 Experiment Setup

The present study investigated the wake behind a torus and the drag of a torus. The experiment setup is divided into two parts. The velocity behind the torus was measured by a hot-wire system. The drag of the torus was obtained by a load cell.

The experiment was conducted in a closed-loop wind tunnel with a 1.8 m long, 7.6 m high, and 7.7 m wide test section. The maximum free stream velocity in the empty test section was around 30 m/s. The flow quality was tested at U_∞=7.8 m/s with an empty test section; the background turbulence intensity was around 0.5%, and the velocity outside the boundary layer varied no more than ±0.2 m/s.

A torus with a core diameter of 17 mm and a mean diameter of 51 mm was used in this study. The torus was made of PVC material and polished by 600-grit sandpaper.

4.2.1 Hot-wire System

In this part, the torus was set in the middle of the cross section of the wind tunnel by 0.2 mm diameter fishing lines. A schematic of the experimental setup is shown in Figure 4. 2. The center of the torus was set as the coordinate origin, and the X-Y-Z axis direction is shown in Figure 4. 3.

Velocity measurements were obtained by a hotwire system which consisted of a single regular hot-wire probe (type 55P11), a temperature probe, a Dantec streamline 55C90 constant-temperature anemometer (CTA), an A/D converter, a 2-D traverse system, and a computer. The traverse system was located at different downstream locations (X/d=5, 7, 10 and 15) of the torus to support the probe. A sampling frequency of 80 kHz with a sampling time of 125 s resulting in 106 samples was set at each measuring location. A controlled 2D traverse system was used to position the probe at each specified location.

The computer-controlled traverse system could move in the widthwise (Y) and the normal (Z) directions. The experiment was conducted at three different free stream velocities, 7.8 m/s, 10.3 m/s, and 13.3 m/s. The Reynolds numbers based on the free stream velocity and core diameter (d) were around 9×103, 1.2×104 and 1.5×104, respectively.
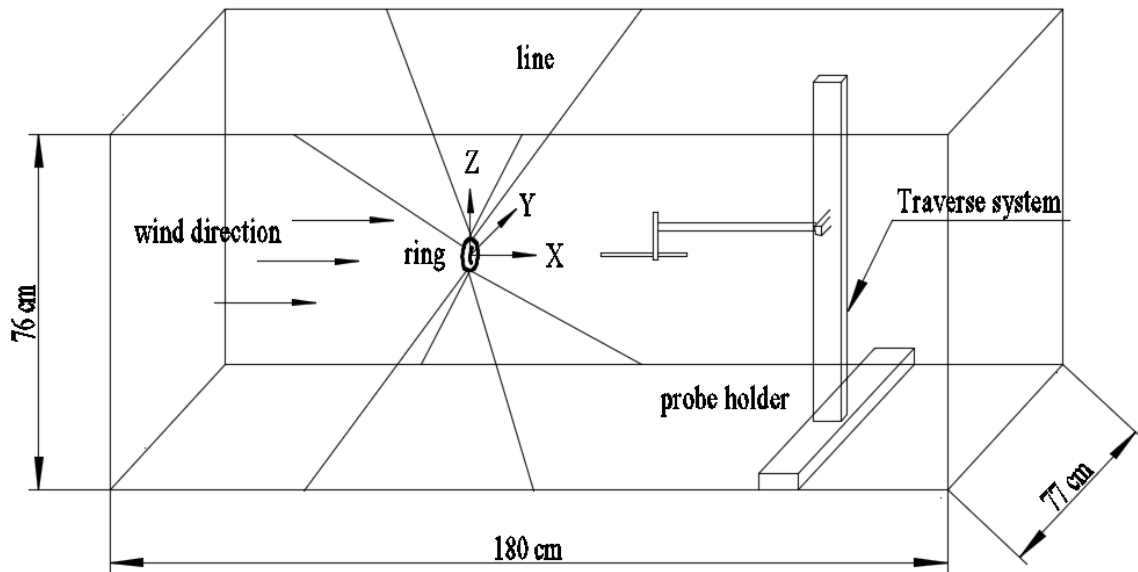
Figure 4. 2 Experiment setup in wind tunnel.

This experiment initially measured the streamwise velocity along the Y and Z centerlines from -112 mm to 112 mm with 4 mm steps at each downstream location (X/d = 5, 7, 10 and 15). Preliminary measurements showed that the velocity distribution at X/d = 5 plane is very similar to that at X/d = 7 plane. Likewise, the velocity profile at X/d = 10 closely represent that at X/d = 15. On the other hand, the near wake (X/d= 5 & 7) velocity contours are different from that of the far wake (X/d = 10 & 15). In addition, the self-similarity of the velocity distributions among the range of the current free stream velocities was also detected. To have a better understanding of the wake structure, this experiment also examined the velocity distribution on a surface instead of just one line. Due to the similarity findings, this experiment just measured the velocity distributions of two planes

(X/d=5 and X/d=10) at a free stream velocity equal to 7.8 m/s. At each plane, velocities were measured through 20 rows × 20 columns, resulting in 400 points. The points were positioned symmetrically along the Y and Z centerlines and were spaced 8 mm apart.

4.2.2 Drag Coefficient Measurement

This experiment used an ATI SI-65-5 load cell to measure the drag force on the torus. This load cell has a resolution of 1/80 N with a 65 N range in the x, y directions and a resolution of 1/40 N with a 200 N range in the z direction. The supporting mechanisms are shown in Figure 4. 3. Three rods (L = 0.4 m, D= 0.003 m) were fixed to the load cell, which was installed inside a shell (protective cylinder). The rods extended out to support the torus (three holes were drilled in the torus to connect with the rods). These three rods can transfer the drag force exerted on the torus to the load cell. The shell protects the load cell from the inlet flow so that the inlet flow does not exert a pushing force on the load cell. Therefore, ideally, the data measured by the load cell is the force (F) experienced by the torus (F_t) and the supporting rods (F_r). To find the magnitude of the drag force acting on the rods, the torus was uncoupled from the rods and held just in front of the rods using 0.2 mm fishing line (Figure 4. 4). The rod did not make contact with the torus. In this scenario, the flow past the rods is almost the same as previously, but the load cell only measured the force (F_r) experienced by the rod. Therefore, the force of the torus can be expressed as $F_t = F - F_r$. It needs to be mentioned that the torus was observed to vibrate slightly in a random manner. The drag was measured with a sampling frequency of 100 kHz with a measuring time of 120 s resulting in 1.2×10^6 samples. The measured drag force was the average value of 1.2×10^6 measuring samples. Thus, the random vibration disturbance could balance out. The drag data was acquired a total four individual measurements and the repeated experiments

showed that the uncertainty of the measured data is around 9.3%. This experiment measured the drag force of the torus at a Reynolds number of 9×10^3, 1.2×10^4 and 1.5×10^4.
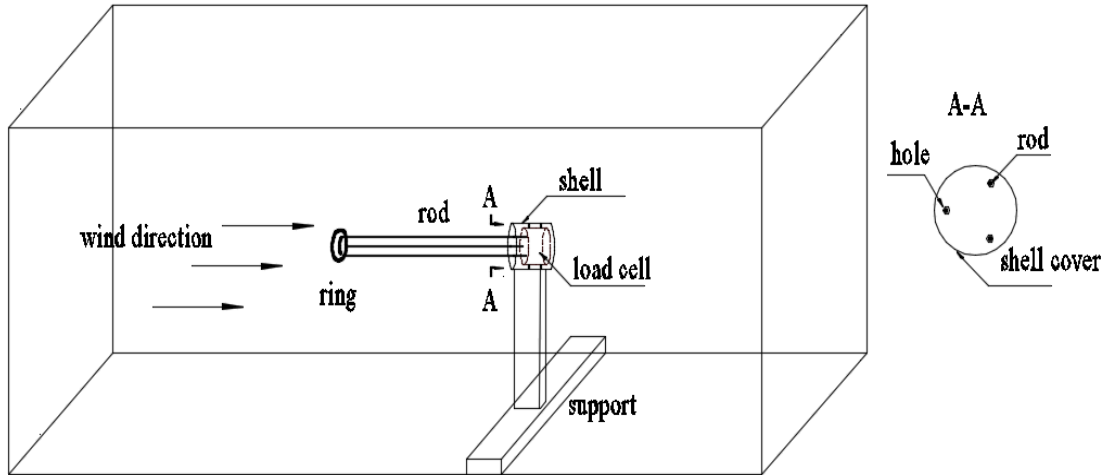
Figure 4. 3 Schematic of the load cell setup with the torus supported by rods.
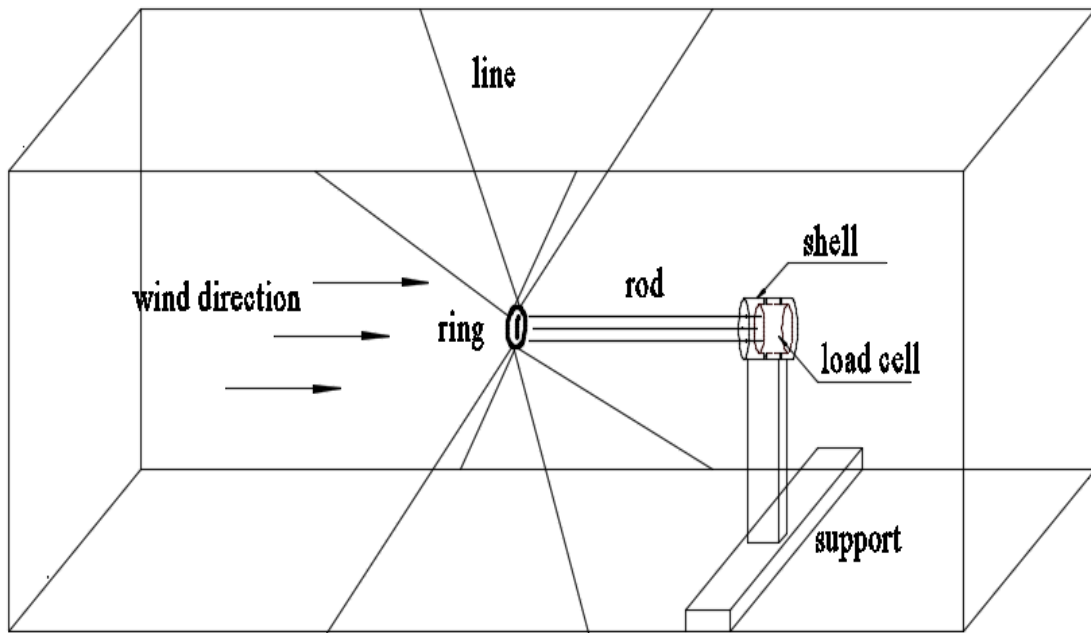
Figure 4. 4 Schematic of the load cell setup measuring the force experienced by rods.

4.3 Hot-wire Data Analysis

The voltage was converted to velocity based on calibration. These velocities were

instantaneous velocities at each point. A Matlab program was used to deduce the following parameters.

Mean velocity is the time-averaged velocity at that particular location. It was calculated as

$$\bar{U} = \frac{1}{N}\sum_{i=1}^{N} U_i \qquad (4.1)$$

where U is the instantaneous velocity and N is the sampling number ($N=10^6$).

The root mean square velocity (u_{rms}) at a particular location was calculated by

$$u_{rms} = \sqrt{\sum_{i=1}^{N} \frac{(U_i - \bar{U})^2}{N-1}} \qquad (4.2)$$

The turbulence intensity indicates turbulence as a percentage of the total energy. Then relative turbulence intensity (Tu) was the normalized standard deviation.

$$Tu = \frac{u_{rms}}{U_\infty} \qquad (4.3)$$

Integral length scale (Λ) represents the large and energy-containing eddies in turbulent flow. Integral time scale can be estimated from the autocorrelation factor (ρ)

$$\rho(\tau) = \frac{\overline{u(t)u(t+\tau)}}{\overline{u^2(t)}} \qquad (4.4)$$

For discrete samples, it would be

$$\rho(k\Delta t) = \frac{\frac{1}{N-m}\sum_{i=1}^{N-k}(u_i u_{i+k})}{\frac{1}{N}\sum_{i=1}^{N} u_i^2} \qquad (4.5)$$

where k is varied from 0 to $N-1$. The integral time scale is

$$\tau_\Lambda = \int_0^\infty \rho(\tau)d\tau \qquad (4.6)$$

The integral time scale (τ_Λ) for discrete samples was

$$\tau_\Lambda = \sum_{i=1}^{N-1} \rho(i\Delta t)\Delta t \qquad (4.7)$$

The Taylor frozen hypothesis [22] states that the eddies can be considered merely flowing over the probe without any evolution if the velocity fluctuation is small compared with the mean flow that carries the eddies. Then the integral length scale can be deduced

by multiplying the integral time scale with the local mean velocity

$$\Lambda = \overline{U} \times \tau_\Lambda \tag{4.8}$$

Taylor microscale (λ) represents the small dissipative eddies in the turbulent flow. Taylor time scale (τ_λ) can be expressed as

$$\tau_\lambda = \sqrt{\frac{\overline{2u^2}}{\overline{\left(\frac{du}{dt}\right)^2}}} \tag{4.9}$$

In the case of discrete samples, it was modified to

$$\tau_\lambda = \sqrt{\frac{\frac{1}{N}\sum_{i=1}^{N} 2u_i^2}{\frac{1}{N-1}\sum_{i=1}^{N-1}\left(\frac{u_{i+1}-u_i}{\Delta t}\right)^2}} \tag{4.10}$$

Similar to the calculation of integral scale, the Taylor microscale (λ) can be obtained via Taylor's frozen hypothesis

$$\lambda = \overline{U} \times \tau_\lambda \tag{4.11}$$

The uncertainty of these parameters is calculated in the Appendix A.

4.4 Results and Discussion

4.4.1 Velocity Profile

The normalized streamwise velocity contour at 85 mm (5d) and 170 mm (10d) downstream of the torus at $U_\infty = 7.8$ m/s (Re= 9×10^3) are shown in Figure 4. 5. The small effect of the supporting fishing line can also be distinguished in the picture. As can be seen, the velocity profile is approximately symmetric to the axis of the torus ($z = 0$).
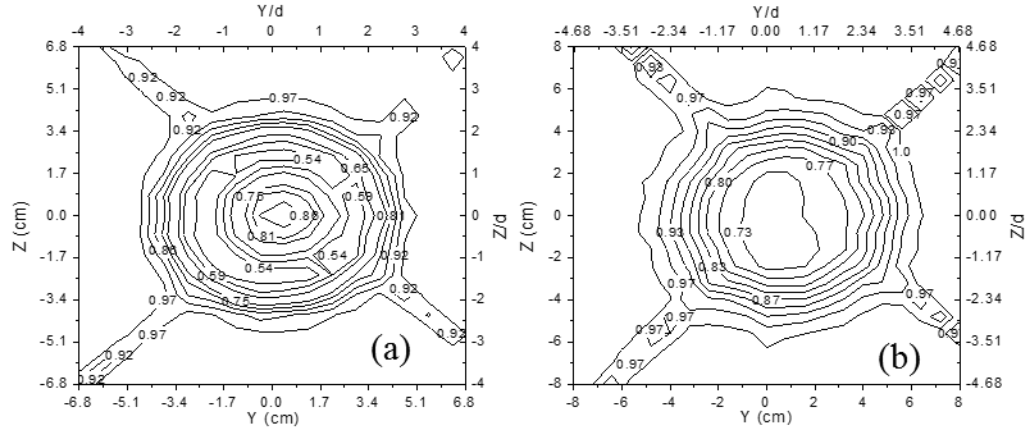
Figure 4. 5 Contours of normalized velocity profiles (U/ U∞) at (a) X = 5d and (b) X = 10d downstream with Re = 9×10³.

Figure 4. 6 shows the stream-wise velocity profiles along the Z-axis at four different downstream distances (X/d = 5, 7, 10 and 15) at Re = 9×10^3. A second vertical axis on the right side of the graph shows the dimensionless distances in the normal direction (Z/d). The schematic diagram of the torus (cross section) position is also shown in the illustration. For X/d = 5, the velocity profile has two lower regions. From the torus center to the radial direction, the velocity decreases, reaching a minimum almost right behind the center of the solid portion of the torus (Z/d = 1.5), beyond which, the velocity recovers gradually to the free stream value at Z/d ≈ 3. The velocity profile at X/d = 7 has a similar trend to X/d = 5, but with a lesser velocity deficit and a more gradual recovery. Farther downstream, the velocity profile becomes different from that of the adjacent locations. The minimum value behind the solid portion of the torus disappeared, and the velocity profile only has one minimum at the center of the torus. As a result, the torus has a block effect on the flow; and the influence of the torus on the flow decreases as downstream distances increase. The maximum uncertainty in normalized time-average velocity is ±0.4 m/s.

In addition, the velocity behind the torus tube (Z/d = ±1.5) for X/d = 5 is smaller than

5 m/s. Therefore, some measuring points experienced directional ambiguity issues and had a larger uncertainty.
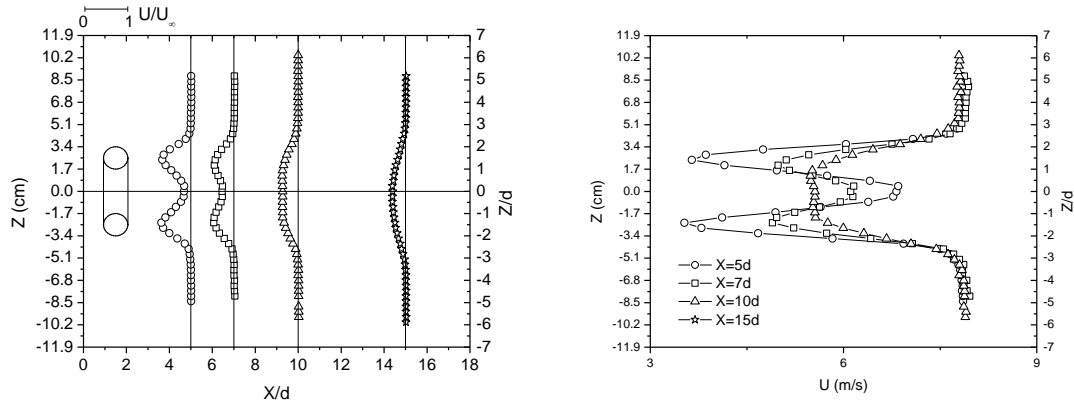
Figure 4. 6 Velocity profile at different downstream distances with Re $= 9 \times 10^3$ (Left: normalized velocity profile, right: dimensional velocity profile).

Figure 4. 7 illustrates the velocity distributions of three different Reynolds numbers. Over the range of studied conditions, the normalized velocity profile generally collapses onto one profile. This depicts the self-similarity of the velocity profile over the range of tested conditions. This self-similarity is more obvious at X/d = 7 and beyond. In other words, it takes about five ring diameters before self-similarity is achieved.
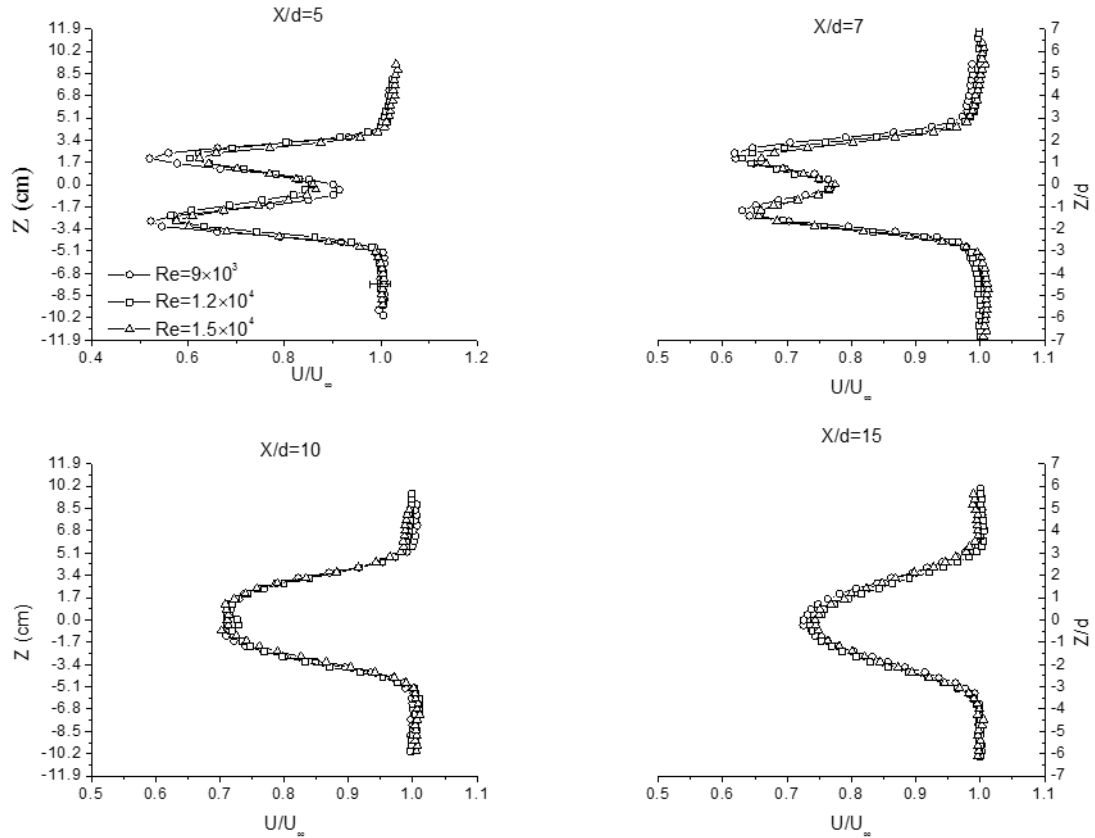
Figure 4. 7 Velocity profiles at different downstream locations with different Reynolds numbers.

4.4.2 Turbulence Intensity

The local turbulence intensity is an indicator of the amount of turbulent kinetic energy available to enhance mixing. It depicts the turbulence level of the flow. The turbulence intensity profile along Z-axis at the four studied downstream locations at Re = 9×10^3 are shown in Figure 4. 8. For X/d = 5: from center to radial direction, the turbulence intensity increases to the first extremum value around 23% at Z/d ≈ 1, then it decreases with almost the same slope to Z/d = 1.5. After that, the turbulence intensity increases to another extremum at Z/d ≈ 2. Since then, the turbulence intensity decreases significantly to free stream turbulence intensity (~0.5%). These two extremums' locations correspond to the maximum velocity gradients in Figure 4. 5. The turbulence intensity profile for X/d = 7 has

a trend that is similar to X/d = 5. However, the position of near center peak turbulence

intensity gets closer to the center, while the center turbulence intensity becomes bigger for

X/d = 7. This signifies that the turbulence in the center is still being generated. However,

the turbulence intensity profile changes farther downstream. Only one extremum from

center to radial direction can be distinguished at the maximum velocity gradient positions.

The near center peak value (Z/d ≈ 1) disappears. This is because the wake structure

gradually deforms and mingles with the inlet flow through the hole.
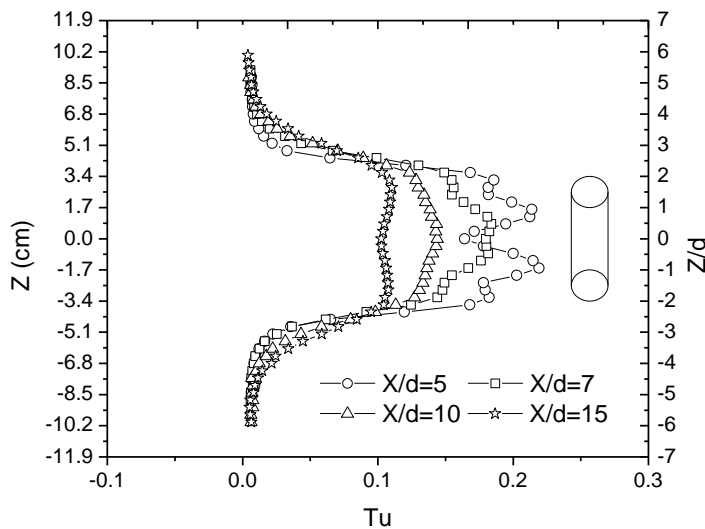
Figure 4. 8 Turbulence intensity at different downstream locations with Re = 9×10^3.

  By comparing the turbulence intensity profile with the velocity profile, it can be seen

that the turbulence intensity profile peaks at the position of the maximum velocity gradient.

This suggests that the turbulence intensity is produced by shear, i.e. velocity gradient. In

addition, the turbulence intensity can be transferred from one region to another. As seen

from Figure 4. 8, a general tendency of decreasing turbulence intensity with the distances

demonstrates can also been observed. It signifies that turbulence decays. Analysis of the

turbulence intensity at different locations downstream of the torus shows a gradual increase

in the extent of the torus wake with distance, signifying that the wake of the torus slightly grows in size with distance downstream.

The turbulence intensity at different Reynolds numbers is shown in Figure 4. 9. The turbulence intensity profile almost remains the same as the Reynolds number increases. This shows the self-similarity over the range of tested conditions. The maximum uncertainty in turbulence intensity is estimated to be $\pm$ 0.4%.
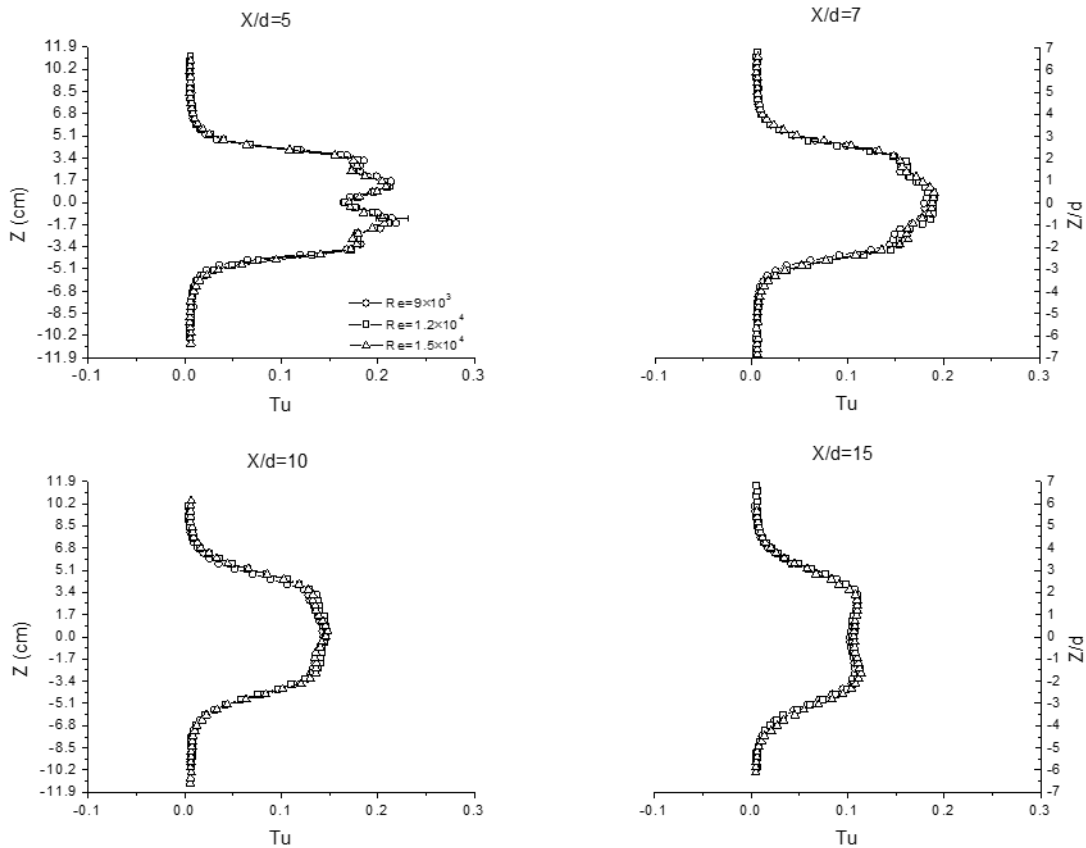
Figure 4. 9 Turbulence intensities at different downstream locations with three different velocities.

4.4.3 Fourier Transform

To catch the large vortex shedding in the shear layer downstream of the torus, a Fast Fourier Transform (FFT) analysis is applied to the velocity fluctuation signals. The shedding frequency is expressed in dimensionless Strouhal number $St = fd/U_\infty$. The

shedding patterns at different velocities at X/d = 5 and X/d = 15 are shown in Figure 4. 10. The dimensionless frequency distribution is symmetric to the Z-axis. We detected two regions each with a different Strouhal number for X/d = 5. The higher Strouhal number occurs in torus opening hole area, and the lower one is found at Z/d = 2~4 or -2~-4. However, only the small Strouhal number is distinguished for X/d=15 (Z/d = 2~4 or -2~-4) while the higher Strouhal number diminishes. Similar phenomenon also happens to the sphere. The sphere has two shedding Strouhal numbers for a specific range of Reynolds number (around $10^3 <$Re$< 10^4$). The higher shedding frequency accounts for the small-scale instability of the separating shear layer, which usually happened at the extreme neighbourhood of a sphere. The lower frequency is the large-scale instability of the wake, which is commonly referred to as vortex shedding frequency [23]. Therefore, it is possible that the high frequency in the current study may also result from the pulsation of the inner shear layer. That is why the high shedding frequency can only be distinguished in the extreme neighborhood of the torus (X = 5d), which is close to the shear layer region.
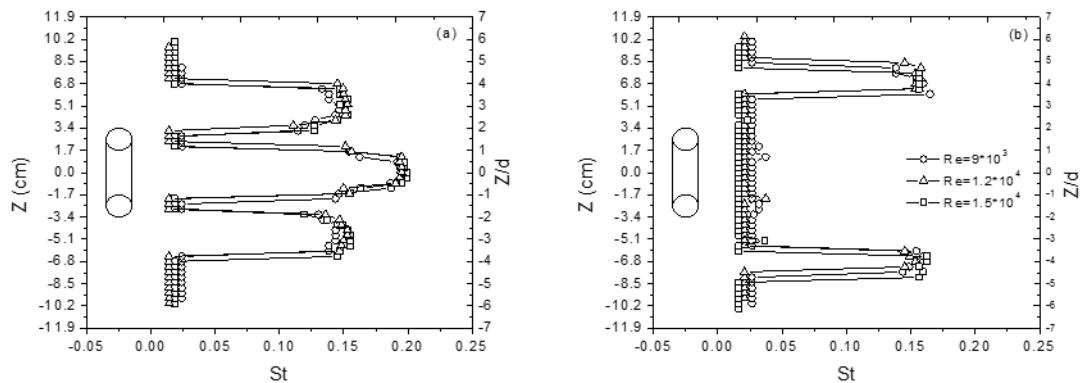
Figure 4. 10 Vortex shedding frequencies at (a) X/d = 5, (b) X/d = 15. The circles signify Re = 9×10^3, the square signifies Re = 1.2×10^4, and the triangles signifies Re=1.5×10^4.

The low Strouhal number is observed near the positions where the Tu is at its maximum (Figure 4. 8). This seems to indicate the presence of the large-scale vortical

structures. The position at which we measured the low Strouhal number is at the same location where Inoue et al. [9] detected the single distinct frequency of the same Ar = 3 torus with a different Reynolds number (Re = 1500). They attributed their shedding frequency to oblique loop structures shed from the torus [9]. Therefore, the large-scale vortical structure in the present study may be also consist of oblique loops, and this low Strouhal number is the vortex shedding frequency. The present vortex shedding frequency (St = 0.15) is smaller than that measured by Inoue et al. (St = 0.2), while our tested Reynolds number is larger than their Reynolds number. The difference may be because the flow changes from laminar to turbulent conditions. The dissipation rate of the energy increases when the flow is turbulent so that it needs more time to store the energy for vortex shedding. After the flow becomes completely turbulent, the Strouhal number becomes almost constant (S = 0.15 for Re = 9×10^3 ~ 1.5×10^4). The phenomenon of shedding frequency becoming smaller as the flow transitions from laminar to turbulent also occurs with spheres [23].

The power spectra of the U-fluctuation at Z = 3d and Z = 0 for X/d = 5 downstream location are shown in Figure 4. 11. At the same measuring location, the Strouhal numbers remains constant as the Reynolds number increases (St ≈ 0.15 for Z/d = 3, and St ≈ 0.19 for Z = 0). The spectral peak for Z/d = 3 was smaller and much broader than that for Z = 0 at the same Reynolds number. This seems to indicate the pulsation of the shear layer is intense. In addition, the amplitude of the peak increases with the Reynolds number.
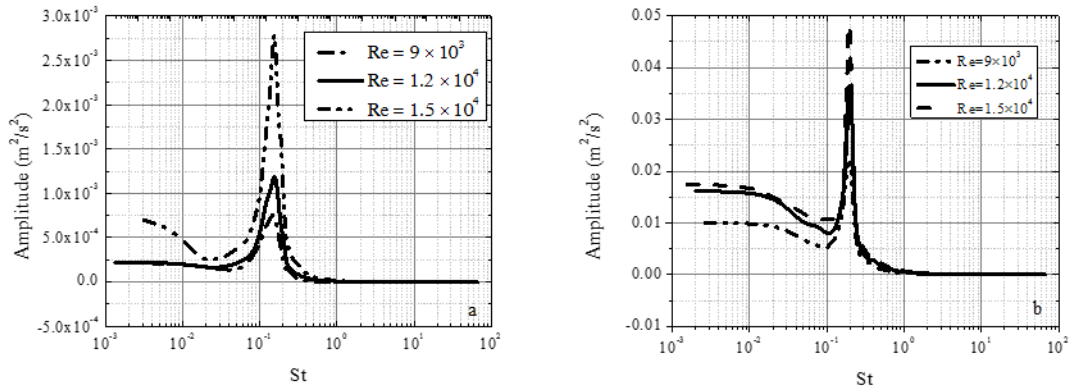
Figure 4. 11 Power spectra of the U-fluctuation at (a) X/d = 5, Z/d = 3, (b) X/d = 5, Z/d = 0
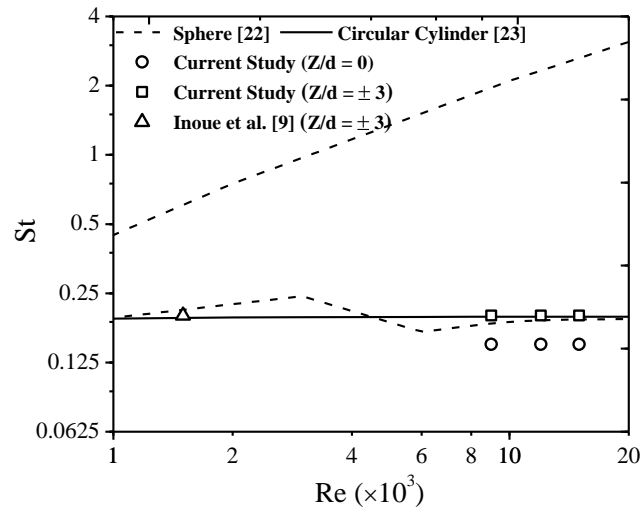
Figure 4. 12 Strouhal number versus Reynolds number.

The present data are compared with the Strouhal number profile for the sphere [23] and the circular cylinder [24] at Re = $8 \times 10^2 \sim 2 \times 10^5$ (shown in Figure 4. 12). Figure 4. 12 also includes the Strouhal number measured by Inoue et al. [9]. They used the Ultrasound Doppler Velocity Profiling (UVP) method to detect the shedding frequency of a torus with Ar = 3 at Re = 1500. Our low shedding frequency is closer to the sphere shedding frequency. This further confirmed that the wake of a torus with the aspect ratio lower than 3.9 is more similar to that of a sphere. It can also be seen from the figure that Inoue et al. [9] did not

detect the high shedding frequency inside the torus hole region of the torus. This is conceivable given that their Reynolds number is lower than the present study. Thus, their shear layer did not pulsate and generate the small-scale instability.

4.4.4 Turbulence Length Scales

A turbulent flow contains a wide range of eddies interacting with each other. There is a continuous transport of energy from mean flow to large eddies, from which energy is transported to a series of increasingly smaller eddies, and this is termed the cascade process. Thus, turbulence motion occurs over a wide range of turbulence scales. These turbulence scales play an important role in the energy and momentum transportation of the flow. To better visualize the range of different eddy sizes, two common scales are studied: the integral length scale, which is an indication of the large energy containing eddies, and the Taylor microscale, which represents small, dissipative eddies.

4.4.4.1 Taylor Microscale

The Taylor microscale represents the size of small, dissipative eddies. Figure 4. 13 shows the normalized Taylor microscale (λ/d) for various occasions. The high turbulence in the wake will drive the energy cascade to dissipate energy to a very small scale. As a result, locations with high-energy dissipation (high turbulence) will have small Taylor microscales and vice versa. For the adjacent downstream areas (X/d = 5 and 7), the Taylor microscale has a higher value in the center of the torus area. As the distance moving away from the center in the radial direction, the Taylor microscale shows a decrease and then an increasing trend at the rear of the torus tube, corresponding to a higher turbulence intensity area. Above the torus, the Taylor microscale decreases dramatically because the free stream has little turbulence (Tu<0.05%). A comparison of the profile of X/d = 5 and X/d = 7

demonstrates that the Taylor microscale near the axis decreases and the Tu increases. This further confirms that the turbulence continues to be generated in the center of this area. For far downstream locations (X/d = 10 and 15), the Taylor microscale profile changed, and only one minimum value occurs in the center. This signifies the transition of the wake structure.
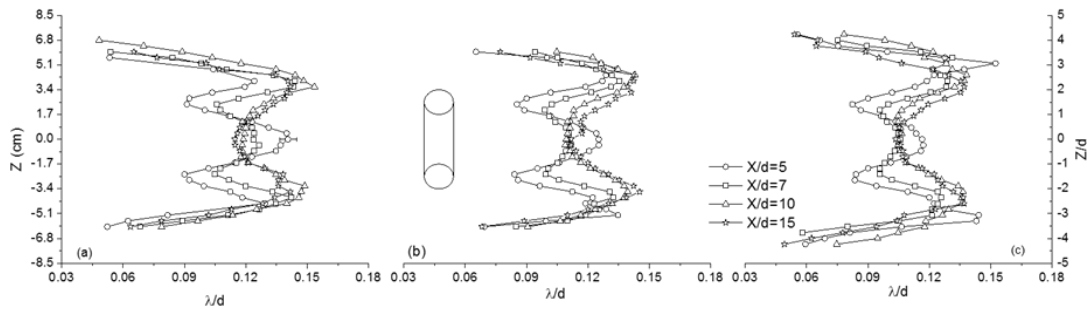
Figure 4. 13 Taylor microscale (normalized by d) at different locations (a) Re = 9×10^3, (b) Re = 1.2×10^4 and (c) Re = 1.5×10^4.
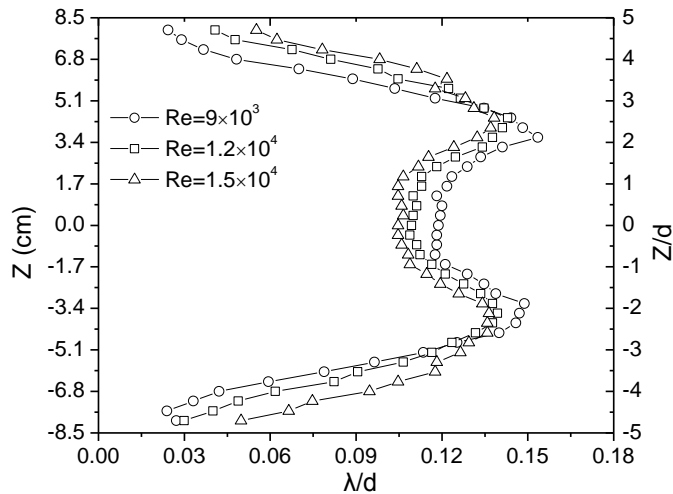
Figure 4. 14 Taylor microscale (normalized by d) with different Reynolds numbers at X/d = 10.

This paper also compares the Taylor microscale at various velocities (Figure 4. 14). A general decrease in eddy sizes occurs with increasing velocities. However, this increasing trend may not be accurate because the maximum uncertainty is estimated to be ± 0.008.

4.4.4.2 Integral Scale
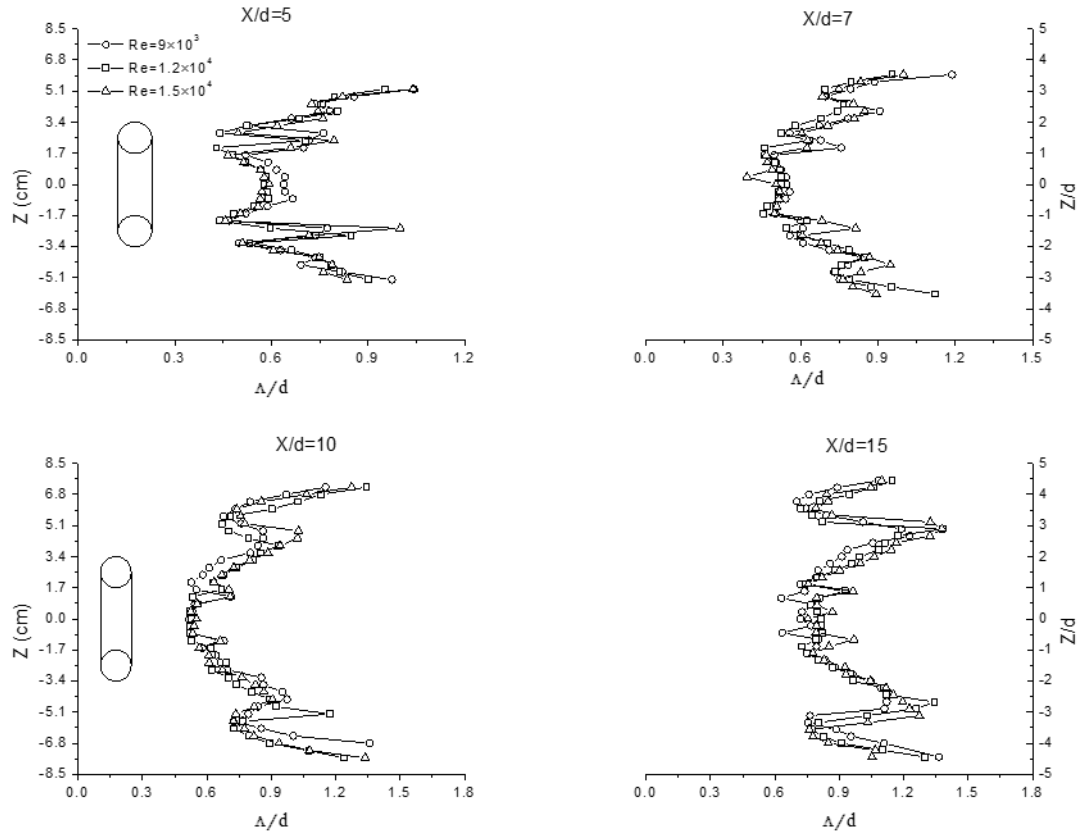
Figure 4. 15 Integral scale at different downstream locations with different Reynolds numbers.

The integral scales that were far from the torus in the radial direction were not calculated since free stream has little turbulence. Therefore, the integral scale is only deduced when the turbulence intensity is larger than 1%. The integral scale profiles along the Z-axis are shown in Figure 4. 15. The integral scale increases slightly with the velocity. From the torus center to the radial direction, the integral scale has two peak values. As downstream distance increases, the near center peak value comes close to the center. At this time, the peak value far from the center became larger. The location of the peak value, which is far from the center, is the same as the position where we measured the low shedding frequency (Figure 4. 10). Therefore, this peak integral scale seems to represents

70

the region of the large-scale wake structure (vortex loop structure) behind the torus. As the downstream distances increases, it is observed that the width and the radial location of the far center peak increases. This signifies the deformation of the vortex loop structure. It floats away from the center and become larger and obscure. However, the accuracy of this conclusion could be compromised by the maximum uncertainty of the integral length scale at this location, around ±0.3 cm.

The integral scale at same free stream velocity with different downstream locations is shown in Figure 4. 16. It shows a trend of increasing integral scale with the downstream locations, signifying the decay of the turbulence downstream.
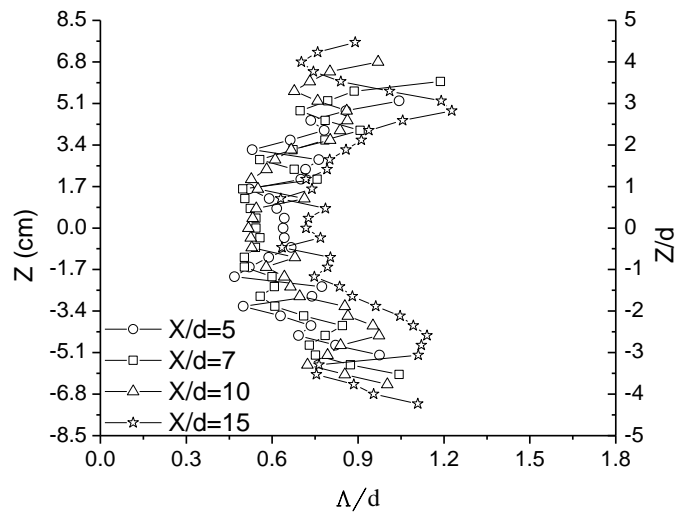
Figure 4. 16 Integral scale at different downstream locations with Re = 9×10^3.

4.4.5 Drag Coefficient

Intuition intimates that a torus will have a less pressure loss, thus leading to a less drag in the flow. Therefore, it is reasonable to believe that a torus will be an ideally suited to replace an orifice disc in a flow meter. To verify this hypothesis, drag measurements were carried out. The drag coefficient (C_D) can be deduced from

$$C_D = \frac{2F_t}{\rho_{air}U_\infty^2 \pi dD}$$
(4.12)

where ρ_{air} is the density of the air. The uncertainty analysis is calculated in the appendix. The drag coefficient of the torus at the current experimental conditions is 0.86, 0.88 and 0.89 respectively with the maximum relative uncertainty around 11.4%. The drag coefficient of the torus was compared with that of a cylinder and a sphere in terms of the Reynolds number. It can be seen from Figure 4. 17, the value of the torus drag coefficient was between that of a sphere and a circular cylinder. In the current torus aspect ratio (Ar = 3), the drag coefficient is closer to a circular cylinder than a sphere.
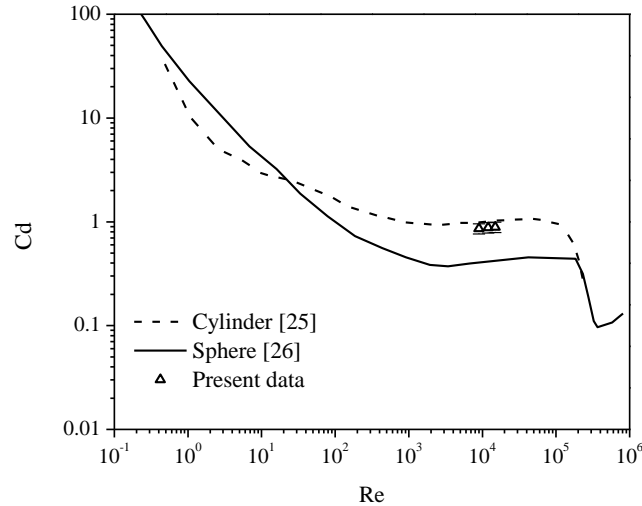
Figure 4. 17 The drag coefficient versus the Reynolds number.

The present data was also compared with the drag coefficient of holed disks in the range of Re = 1.3×10^4 ~ 6.8×10^4. It can be seen from Figure 4. 18, the drag coefficient of a torus is much smaller compared to a holed disc at the same aspect ratio at almost the same range of the Reynolds number. This is attributed to the round edge of the torus. By comparing the wake of torus studied by Sheard et al. [1, 12, 13] with that of a holed disk studied by Bearman & Tokamoto [15] and Miau et al. [27], we found the wake structure of a torus and a holed disk is almost the same. From our study, we found that the torus shape

has s smaller drag coefficient.

The torus restricts the flow so that the pressure before and after the torus is different. This pressure difference can be measured using pressure gauges to determine the flow rate. In addition, the drag coefficient of the torus is much smaller than that of an orifice disc. As a result, we can use a torus to replace the holed disc for a flow meter. It has all the advantages of orifice flow meter. Moreover, the torus shape will lead to a smaller pressure loss.
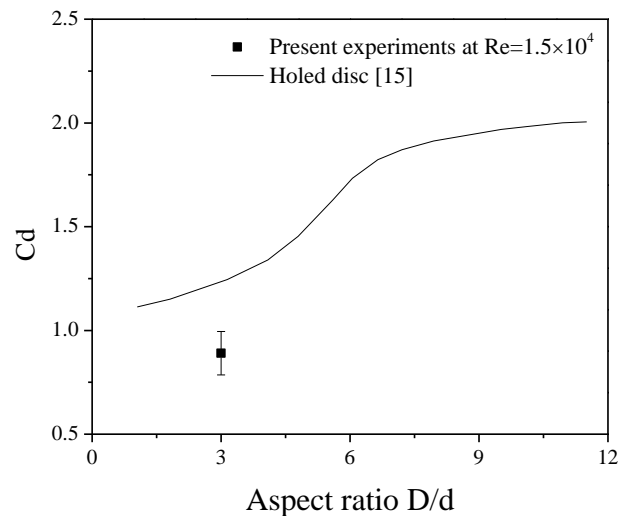
Figure 4. 18 The drag coefficient versus the aspect ratio.

4.5 Conclusion

This paper investigated the flow patterns of the torus with Ar = 3 through a Reynolds number range from 9×10^3 to 1.5×10^4 using hot-wire measurements. Two vortex shedding frequencies can be detected over this studied range of Reynolds number. The low shedding frequency is the vortex shedding frequency of the torus. The high shedding frequency is possibly driven by the pulsation of the shear layer. The vortex shedding frequency almost remains constant over the experimental conditions considered here. The pressure is different before and after the torus, so that the torus can also be used to measure the flow

rate. In addition, the drag coefficient of the torus is much smaller than that of an orifice disc. Therefore, a torus shape could be a substitution for the orifice disc in an orifice flow meter due to its reduced pressure loss.

Acknowledgements

References

[1] G.J. Sheard, M.C. Thompson, K. Hourigan, From spheres to circular cylinders: the stability and flow structures of bluff ring wakes, J. Fluid Mech. 492 (2003) 147-180.

[2] M. Horowitz, C.H.K. Williamson, The effect of Reynolds number on the dynamics and wakes of freely rising and falling spheres, J. Fluid Mech. 651 (2010) 251-294.

[3] M. Ozgoren, Flow structure in the downstream of square and circular cylinders, Flow Meas. Instrum. 17 (2006) 225-235.

[4] K. Liu, J.D. Deng, M. Mei, Experimental study on the confined flow over a circular cylinder with a splitter plate, Flow Meas. Instrum. 51 (2016) 95-104.

[5] G.S. Manning, Null-DNA: A Theory of the elastic instability and spontaneous kinking of DNA with charge-neutralized phosphates, in: C. Nicolini (Ed.), In Structure and Dynamics of Biopolymers, Springer, Netherland, pp. 169-187.

[6] L.M. Bergström, Thermodynamics and bending energetics of torus like micelles, J. Colloid Interface Sci. 327 (2008) 191-197.

[7] F. Springer, E. Carretier, D. Veyret, P. Moulin, Developing lengths in woven and helical tubes with dean vortices flows, Eng. Appl. Comp. Fluid 3 (2009) 123-134.

[8] A. Roshko, On the development of the turbulent wakes from vortex sheets, NACA Report 1911, (1954).

[9] Y. Inoue, S. Yamashita, M. Kumada, An experimental study on a wake behind a torus using the UVP monitor, Exp. Fluids, 26 (1999) 197-207.

[10] Y. Wang, C. Shu, C.J. Teo, L.M. Yang, An efficient immersed boundary-lattice

Boltzmann flux solver for simulation of 3D incompressible flows with complex geometry, Compt. Fluids, 124 (2016) 54-66.

[11] P. Yu, Steady flow past a torus with an aspect ratio less than 5, J. Fluids Struct. 48 (2014) 393-406.

[12] G.J. Sheard, M.C. Thompson, K. Hourigan, On axisymmetric bluff body wakes: Three-dimensional wake structures and transition criticality of the torus, in: 3rd Bluff Body Wake and Vortex-induced Vibrations Conf. 2002.

[13] G.J. Sheard, M.C. Thompson, K. Hourigan, From spheres to circular cylinders: non-axisymmetric transitions in the flow past rings, J. Fluid Mech. 506 (2004) 45-78.

[14] D.R. Monson, The effect of transverse curvature on the drag and vortex shedding of elongated bluff bodies at low Reynolds number, J. Fluids Eng. 105 (1983) 308-318.

[15] P.W. Bearman, M. Takamoto, Vortex shedding behind rings and discs, Fluid Dyn. Res. 3 (1988) 214-218.

[16] T. Leweke, M. Provansal, The flow behind rings: bluff body wakes without end effects, J. Fluid Mech. 288 (1995) 265-310.

[17] C.H.K. Williamson, The existence of two stages in the transition to three-dimensionality of a cylinder wake, Phys. Fluids 31 (1988) 3165-3168.

[18] Y.D. Huang, B.M. Zhou, Z.L. Tang, Instability of cylinder wake under open-loop active control, Appl. Math. Mech. 38 (2017) 1-14.

[19] H.Q. Zhang, U. Fey, B.R. Noack, M. König, H. Eckelmann, On the transition of the cylinder wake, Phys. Fluids 7 (1995) 779-794.

[20] G.J. Sheard, M.C. Thompson, K. Hourigan, T. Leweke, The evolution of a subharmonic mode in a vortex street, J. Fluid Mech. 534 (2005) 23-38.

[21] F.E. Jørgensen, How to Measure Turbulence With Hot-Wire Anemometers—A Practical Guide, Dantec Dyn., Skovlunde, 2002.

[22] G.I. Taylor, The spectrum of turbulence, Proc. R. Soc. Lond. A 164 (1938) 476– 490.

[23] H. Sakamoto, H. Haniu, A study on vortex shedding from spheres in a uniform flow, J. Fluids Eng. 112 (1990) 386-392.

[24] R.D. Blevins, Flow-induced vibration, second ed., Van Nostrand Reinhold, New York, 1990.

[25] D.A. Chin, Fluid mechanics for engineers, first ed., Pearson, 2016.

[26] N. Moradian, D.S.K. Ting, S. Cheng, The effects of freestream turbulence on the drag coefficient of a sphere, Exp. Them. Fluid Sci. 33 (2009) 460-471.

[27] J.J. Miau, E.G. Chiu, J.H. Chou, Laser-sheet flow visualization of the confined wake behind a ring, Fluid Dyn. Res. 9 (1992) 255-265.

CHAPTER 5 CONCLUSION AND FUTURE WORK

5.1 Conclusion

A propagating vortex ring has a region of fluid spinning around it. This spinning fluid reduces the friction between the vortex core and the surrounding fluid, enabling the vortex ring to travel a long distance with little loss of mass and energy. It can be a favorable medium for transporting mass and energy. In nature, the vortex ring is a basic fluid structure that exists in a wide range of biological, atmospheric, and engineering applications. This thesis investigated the propagation characteristics and the laminar to turbulent transition regime of a buoyant vortex ring. The author also studied the wake structure of a non-rotating (solid core) vortex ring in the wind tunnel.

In chapter 2, a general map of a buoyant vortex ring formation and transition from laminar to turbulent was constructed in terms of the Reynolds number, Bond number and Weber number. For Reynolds number lower than 14,000, Bond number below 30, and Weber number below 70, the vortex ring could not be produced. A transition regime was observed for Reynolds numbers between 40,000 and 65,000, Bond numbers between 120 and 280 and Weber number between 400 and 700. Below this range, only laminar vortex rings were observed, and above, only turbulent vortex rings.

In chapter 3, the effect of the dimensionless surface tension on the flow behaviors of a buoyant vortex ring was studied, including the rising velocity, ring radius, relative core radius, circulation and the energy of the bubble ring. The rising velocity decreases and the ring radius expands. The circulation of the bubble ring almost remains constant. The kinetic energy of the bubble ring continuously increases, while the total potential energy decreases.

The mechanical energy of the bubble ring decreases slightly when the ring rises. The energy decay trend is more obvious as the dimensionless surface tension decreases.

In chapter 4, the wake structure behind a solid core vortex ring with Ar = 3 was studied through a Reynolds number range from 9×10^3 to 1.5×10^4 using hot-wire measurements. The wake structure of the solid core vortex ring consists of oblique vortex loops and the pulsating cylindrical shear layer at the extreme neighborhood. Two vortex shedding frequencies can be detected over this studied range of Reynolds numbers. The low shedding frequency is the vortex shedding frequency. The high shedding frequency is possibly driven by the pulsation of the shear layer. The vortex shedding frequency almost remains constant over the experimental conditions considered here.

5.2 Future Work

As the Bond number, Weber number and Reynolds number increases, the body of the fluid will change from cap bubble to laminar vortex ring to transition to turbulent vortex ring. In theory, if the inertia of a vortex ring is too large, the vortex ring will break into spherical bubbles. Thus, when the Reynolds number, Bond number and Weber number are larger than an upper limit, the vortex ring should disintegrate. Due to the experimental limitations, the study did not obtain this upper limit. Future studies in this area can build a taller water tank to find this limitation. Moreover, the general trend of the transition behavior of the bubble ring is correct. However, the transition regime value may be different with experimental setups (i.e. different generation method). Future studies can also investigate the effect of the experimental setup on the transition map.

The vortex ring is moving, and the ring core is rotating. The present study tried to study the flow behind a bubble ring by assuming that the core is solid and measured the

wake of a solid core vortex ring in the wind tunnel. However, it cannot totally represent the wake of a rotating core vortex ring. The rotating core will also influence the wake. Due to the technology restriction, the wake structure of a bubble ring could not be measured. The future work can try to directly observe the wake of a bubble ring using more advanced technologies.

APPENDIX A: UNCERTAINTY ANALYSIS IN THE HOT-WIRE DATA AND

DRAG MEASUREMENT

The uncertainty is made up of bias error and precision error. The bias error of the hot wire is estimated by Jorgensen [1]. The precision is the degree of reproducibility of the experiment. This can be estimated from repeated measurements. In this study, a Student t distribution method with 95% confidence level was used. The precision of sample mean value equals

$$P = t_{v,p} S_{\bar{x}} \tag{A. 1}$$

As a result, the total uncertainty (W) is

$$W = \sqrt{B^2 + P^2} \tag{A. 2}$$

The uncertainties of $\bar{U}$ and u_{rms} are obtained using the above method. The other corresponding uncertainties are deduced by uncertainty propagation method.

Turbulence intensity can be calculated from Eq. (4.3), and then its uncertainty is

$$W_{Tu} = \frac{u_{rms}}{U_\infty} \sqrt{\left(\frac{1 \times W_{u_{rms}}}{u_{rms}}\right)^2 + \left(\frac{-1 \times W_{U_\infty}}{U_\infty}\right)^2} \tag{A. 3}$$

The uncertainty of the free stream velocity equals to the uncertainty of the mean velocity $W_{U_\infty} = W_{\overline{U_\infty}} = W_{\bar{U}}$. Therefore, Eq. (A. 3) can be written as

$$W_{Tu} = \frac{u_{rms}}{U_\infty} \sqrt{\left(\frac{1 \times W_{u_{rms}}}{u_{rms}}\right)^2 + \left(\frac{-1 \times W_{\bar{U}}}{U_\infty}\right)^2} = \sqrt{\left(\frac{W_{u_{rms}}}{U_\infty}\right)^2 + \left(\frac{u_{rms} \times W_{\bar{U}}}{U_\infty^2}\right)^2} \tag{A. 4}$$

The integral scale is

$$\Lambda = \bar{U} \times \tau_\Lambda = \sum_{i=1}^{N-1} \rho(i\Delta t)\Delta t = \sum_{i=1}^{N-1} \frac{\frac{1}{N-m}\sum_{i=1}^{N-k}(u_i u_{i+k})}{\frac{1}{N}\sum_{i=1}^{N} u_i^2} \Delta t \tag{A. 5}$$

According to Eq. (4.2), we can obtain

$$(N-1) \times u_{rms}^2 = \sum_{i=1}^{N} u_i^2 \tag{A. 6}$$

As a result, Eq. (A. 5) is

$$\Lambda = \bar{U} \times \sum_{i=1}^{N-1} \frac{\frac{1}{N-m}\sum_{i=1}^{N-k}(u_i u_{i+k})}{u_{rms}^2} \Delta t \tag{A. 7}$$

Because $\frac{1}{N-m}\sum_{i=1}^{N-k}(u_i u_{i+k}) \sim \frac{1}{N-m}\sum_{i=1}^{N-k} u_i^2 = u'_{rms}$, then the numerator of the integral scale can be approximately equal to the u_{rms} for N-m terms. Then the integral scale uncertainty is

$$W_\Lambda = \Lambda \times \sqrt{\left(\frac{1 \times W_{\bar{U}}}{\bar{U}}\right)^2 + \sum_{i=1}^{N-1}\left(\left(\frac{-2 \times W_{u_{rms}}}{u_{rms}}\right)^2 + \left(\frac{2 \times W_{u_{rms}}}{u_{rms}}\right)^2\right)\Delta t} \tag{A. 8}$$

Because $\Delta t = 1/N$, then

$$W_\Lambda == \Lambda \times \sqrt{(\frac{W_{\bar{U}}}{\bar{U}})^2 + 2 \times (2 \times \frac{W_{u_{rms}}}{u_{rms}})^2} \tag{A. 9}$$

Using the same approximation method, the uncertainty of the Taylor microscale is

$$W_\lambda = \lambda \times \sqrt{(\frac{W_{\bar{U}}}{\bar{U}})^2 + 2 \times (\frac{W_{u_{rms}}}{u_{rms}})^2} \tag{A.10}$$

The uncertainty of the drag coefficient came primarily from five sources: the ring diameter measurement, the core diameter measurement, the air density estimation, the drag force measurement and the free stream velocity. The diameter of the torus was measured using a caliper whose resolution is 0.0254 mm. Therefore, the uncertainty of the instrument was ±0.0127 mm. The repeated measurement shows a precision uncertainty for the ring radius was around ±0.4 mm and for the core radius was around ±0.3 mm. Thus, the total uncertainty of the ring radius and core radius was 0.7% and 1.1%. The uncertainty of the free stream velocity was 3% as discussed previously. The uncertainty in the air density can be neglected. The maximum uncertainty of a load cell measurement is around 9.3%. Then the drag coefficient uncertainty can be calculated as

$$W_{C_D} = \sqrt{(\frac{W_{F_D}}{F_D})^2 + (-1 \times \frac{W_\rho}{\rho})^2 + (2\frac{W_{U\infty}}{U_\infty})^2 + (\frac{W_D}{D})^2 + (\frac{W_d}{d})^2} \tag{A. 11}$$

As a result, the uncertainty of the drag coefficient is 11.4%.

[1] F.E. Jørgensen, How to Measure Turbulence with Hot-Wire Anemometers—A Practical Guide, Dantec Dyn., Skovlunde, 2002.

APPENDIX B: MATLAB PROGRAM FOR THE BUBBLE RING EXPERIMENT

B. 1 Side Camera Program

The videos from the side camera are first processed using the 'mainprogramzy' program to get the binary image. Then, run 'mainzy' program to obtain the vortex rings' parameters.

B. 1. 1 Mainprogramzy Program

```
close all;clear all;clc;

file_path = 'C:\Users\ecs\Google Drive\video of buoyant vortex ring\Matlab\data\180\';

img_path_list = dir(strcat(file_path,'*.jpg'));

img_num = length(img_path_list);

if img_num > 0

            for jj = 1:4:img_num

                image_name1 = img_path_list(jj).name;

                image1 = imread(strcat(file_path, image_name1));

                    image1=imcrop(image1,[0 120 1280 550]);

                image2=imread('C:\Users\ecs\Google Drive\video of buoyant vortex

ring\Matlab\data\180 11\datazy\180 4 021.jpg');

                image2=imcrop(image2,[0 120 1280 550]);

                jjj=(jj+3)/4 % name the processed picture and save it into the 'datapre'

folder

                fprintf('%d %d %s\n',i,j,strcat(file_path,image_name1));

                D=imabsdiff(image1, image2);

                D=rgb2gray(D);
```

```matlab
            [m2,n2]=size(D);

            for i=1:m2

              for j=1:n2,

                 if D(i,j)>=30;

                     D(i,j)=image1(i,j);

                     %D(i,j)=1;

                 else

                     D(i,j)=0;

                 end

              end

            end

              D=medfilt2(D, [3 3]);

              kk=int2str(jjj);

imwrite(D,strcat('c:\datazy\datapre\',image_name1,kk,'.jpg'));

          end

   end

   image2=imread('c:\datazy\data\260 s 049.jpg');

     imtool(image2);
```

B. 1. 2 Mainzy Program

```matlab
   close all;clear all;clc;

   file_path = 'c:\datazy\datapre\'; % Image folder path

   img_path_list = dir(strcat(file_path,'*.jpg')); % obtain all the 'jpg' format images

   img_num = length(img_path_list); %to get how many images in the folder
```

```matlab
if img_num > 0

        for j = 1:4:img_num

                image_name = img_path_list(j).name;

                image = imread(strcat(file_path, image_name));

                figure

                fprintf('%d %d %s\n',i,j,strcat(file_path,image_name)); % show the
current processed image's name

                    subroutinezy1 % if the image only has a single vortex ring

                  % subroutinezy2 % if the image includes a bubble ring and a pinch-off jet

            end

        save c:\datazy\data\data1

    end

    xlswrite('c:\datazy\2.xlsx', D,'sheet','B');

    xlswrite('c:\datazy\2.xlsx', Oy,'sheet','C');
```

B. 1. 3 Subprogram1 Program

```matlab
    D1=image;

    z=j; scale=0.001719;

    [m,n]=size(D1);

    hold on

    subplot(2,1,1); imshow(D1);

    title('Final Picture')
```

```
threshold=graythresh(D1);

if threshold~=0

D1=im2bw(D1, threshold);

BW=edge(D1,'canny');

L=bwlabel(BW,8);

stats = regionprops(L,'Area');

area = cat(1, stats.Area);

P = max(area);

BW1 = bwareaopen(L,P,8);

BW1= ismember(L, find([stats.Area] >= P));

subplot(2,1,2); imshow(BW1)

[l,n]=bwlabel(BW1,8);%ÖØÐÂÍ¼ÏñÇøÓò±ê¼Ç

hold on

for k=1:n %label the centroid

[r,c11]=find(l==k);

rbar=mean(r);

cbar=mean(c11);

plot(cbar,rbar,'Marker','o','MarkerEdgeColor','k','MarkerFaceColor','k','MarkerSize',10);
```

```
plot(cbar,rbar,'Marker','*','MarkerEdgecolor','w');

end

STATS1 =regionprops(l,'all');

Oxz = STATS1.Centroid; %centroid coordinates

Oy11=Oxz(1,1); Oz11=Oxz(1,2);

S = STATS1.Area;

P1=STATS1.Perimeter;

[x y]=find(BW1);%read the coordinates of the outline of the bubble ring

title('´Final Picture ')

xmin=min(x); xmax=max(x); DD=xmax-xmin;

DD=DD*scale; %outer diameter

data(z).D=DD;

data(z).y=Oy11*scale; %x coordinate of the centroid

data(z).z=Oz11*scale; % y coordinate of the centroild

save c:\datazy\data\datazy

nn=int2str(j);

imwrite(BW1,strcat('c:\datazy\dataend\',image_name,nn,'.jpg'));

else
```

hold on

subplot(2,1,2);imshow(D1)

title('Final picture')

end

B. 1. 4 Subprogram2 Program

scale=0.001545; % depends on the video

D1=image;% z=j;

[m,n]=size(D1);

imshow(D1);

title('Current processing picture')

warning off;

hold on

% cut the image so that the picture only have the bubble ring. The main purpose of this

process is to create a rectangular region which only contains the bubble ring. So click the

mouse twice to get the up left and right bottom of this rectangular. The other parts of the

video wil automatically deleted by the program%

disp('cut the picture');

disp('Click the left button of the mouse to take the upper left point of the cropped image');

[a,b]=ginput(1); plot(a,b,'b+');

disp('Click the left mouse button to take the image to the bottom right of the crop');

[a1,b1]=ginput(1);

plot(a1,b1,'b+'); D1=imcrop(D1,[a b a1-a b1-b]);

```matlab
figure

subplot(2,1,1),imshow(D1);

title('The picture after cutting off')

threshold=graythresh(D1);

if threshold~=0

    D1=im2bw(D1,threshold);

    BW=edge(D1,'canny');

    L=bwlabel(BW,8);

    stats = regionprops(L,'Area');

    area = cat(1,stats.Area);

    P = max(area);

    BW1 = bwareaopen(L,P,8);

    BW1= ismember(L, find([stats.Area] >= P));

    subplot(2,1,2);imshow(BW1)

    [l,n]=bwlabel(BW1,8);

    hold on

    for k=1:n %centroid

        [r,c11]=find(l==k);

         rbar=mean(r);

         cbar=mean(c11);

plot(cbar,rbar,'Marker','o','MarkerEdgeColor','k','MarkerFaceColor','k','MarkerSize',10);

        plot(cbar,rbar,'Marker','*','MarkerEdgecolor','w');

    end
```

```matlab
STATS1 =regionprops(l,'all');

Oyz = STATS1.Centroid; %centroid's coordinate in the cutting off picture

Oy11=Oyz(1,1);

Oz11=Oyz(1,2);

Oy11=Oy11+a;% centroid's coordinate in the original picture

Oz11=Oz11+b;

[x y]=find(BW1);

title('Final Picture')

xmin=min(x);

xmax=max(x);

DD=xmax-xmin;

DD=DD*scale;

data(z).D=DD;

data(z).y=Oy11*scale; %x coordinate of the centroid

data(z).z=Oz11*scale; % y coordinate of the centroild

save c:\datazy\data\datazy

nn=int2str(j);

imwrite(BW1,strcat('c:\datazy\dataend\',image_name,nn,'.jpg'));

else

subplot(2,1,2);imshow(D1)

title('Final Picture')

    end
```

B. 2 Top Camera Program

```
xq=jn

figure

imshow(image); title('Current processing picture')

warning off;

disp('outer diameter，please input four point');

[x11,y11]=ginput(1);

hold on

plot(x11,y11,'r+')

[x12,y12]=ginput(1);

hold on

plot(x12,y12,'r+')

[x13,y13]=ginput(1);

hold on

plot(x13,y13,'r+')

[x14,y14]=ginput(1);

hold on

plot(x14,y14,'r+')

disp('inner diameter,please input four point');

[m11,n11]=ginput(1);

hold on

plot(m11,n11,'r+')

[m12,n12]=ginput(1);
```

hold on

plot(m12,n12,'r+')

[m13,n13]=ginput(1);

hold on

plot(m13,n13,'r+')

[m14,n14]=ginput(1);

hold on

plot(m14,n14,'r+')

x=[x11 x12 x13 x14];

y=[y11 y12 y13 y14];

m=[m11 m12 m13 m14];

n=[n11 n12 n13 n14];

N=4;

x1 = 0; x2 = 0; x3 = 0;

y1 = 0; y2 = 0; y3 = 0;

x1y1 = 0; x1y2 = 0; x2y1 = 0;

for i = 1 : N

    x1 = x1 + x(i); x2 = x2 + x(i)*x(i); x3 = x3 + x(i)*x(i)*x(i);

    y1 = y1 + y(i); y2 = y2 + y(i)*y(i); y3 = y3 + y(i)*y(i)*y(i);

    x1y1 = x1y1 + x(i)*y(i); x1y2 = x1y2 + x(i)*y(i)*y(i); x2y1 = x2y1 + x(i)*x(i)*y(i);

end

C = N * x2 - x1 * x1;

D = N * x1y1 - x1 * y1;

E = N * x3 + N * x1y2 - (x2 + y2) * x1;

G = N * y2 - y1 * y1;

H = N * x2y1 + N * y3 - (x2 + y2) * y1;

a = (H * D - E * G)/(C * G - D * D);

b = (H * C - E * D)/(D * D - G * C);

c = -(a * x1 + b * y1 + x2 + y2)/N;

A = a/(-2);   B = b/(-2);

R = sqrt(a * a + b * b - 4 * c)/2;

x0=A;

y0=B;

r=R;

theta=0:pi/50:2*pi;

xx=x0+r*cos(theta);

yy=y0+r*sin(theta);

plot(xx,yy,'-',x0,y0,'.');

axis equal

hold on,

scatter(x,y)

m1 = 0; m2 = 0; m3 = 0;

n1 = 0; n2 = 0; n3 = 0;

m1n1 = 0; m1n2 = 0; m2n1 = 0;

for j = 1 : N

        m1 = m1 + m(j);

```
        m2 = m2 + m(j)*m(j);

        m3 = m3 + m(j)*m(j)*m(j);

        n1 = n1 + n(j);

        n2 = n2 + n(j)*n(j);

        n3 = n3 + n(j)*n(j)*n(j);

        m1n1 = m1n1 + m(j)*n(j);

        m1n2 = m1n2 + m(j)*n(j)*n(j);

        m2n1 = m2n1 + m(j)*m(j)*n(j);

end

CC = N * m2 - m1 * m1;

DD = N * m1n1 - m1 * n1;

EE = N * m3 + N * m1n2 - (m2 + n2) * m1;

GG = N * n2 - n1 * n1;

HH = N * m2n1 + N * n3 - (m2 + n2) * n1;

aa = (HH * DD - EE * GG)/(CC * GG - DD * DD);

bb = (HH * CC - EE * DD)/(DD * DD - GG * CC);

cc = -(aa * m1 + bb * n1 + m2 + n2)/N;

A1 = aa/(-2);              B1 = bb/(-2);

R1 = sqrt(aa * aa + bb * bb - 4 * cc)/2;

m0=A1;

n0=B1;

rr=R1;

theta=0:pi/50:2*pi;
```

```
xx1=m0+rr*cos(theta);

yy1=n0+rr*sin(theta);

hold on

plot(xx1,yy1,'-',m0,n0,'.');

axis equal

hold on,

scatter(m,n)

data(xq).big_D=R*2;

data(xq).small_d=R1*2;

data(xq).ratio=R1/R;

Ratio=cat(1,data.ratio);

data(xq).x=(A+A1)/2;
```

APPENDIX C: REAL PICTURES OF THE BUBBLE RING EXPERIMENT

The experiment setup is shown in Figure C. 1. The bubble ring picture is shown in Figure C. 2.
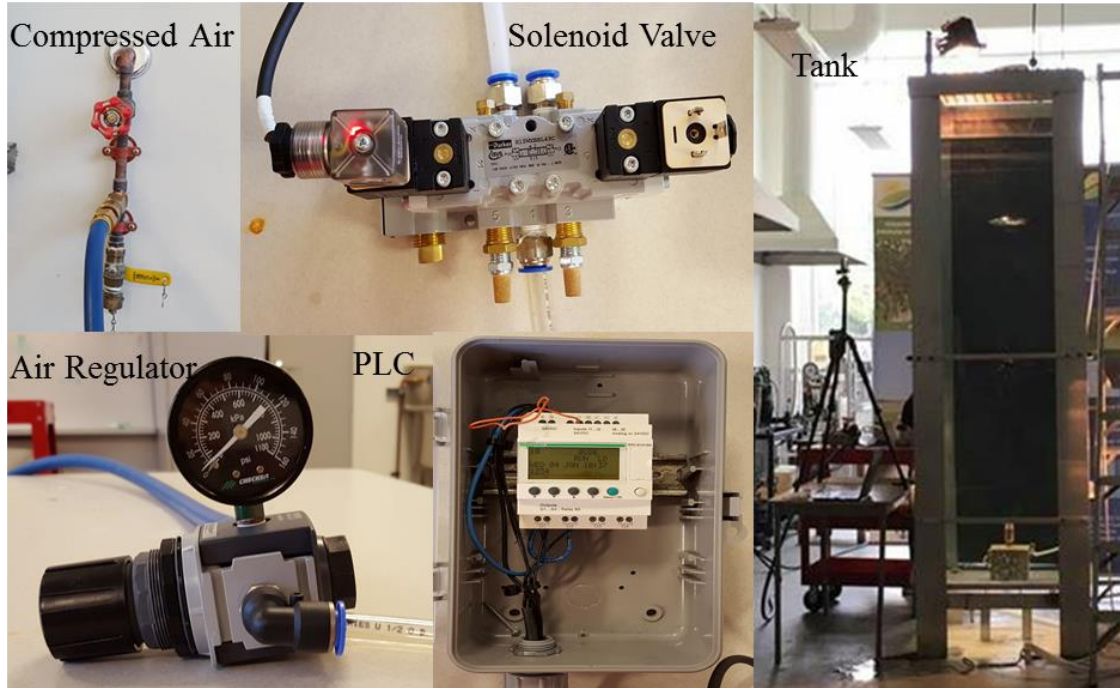
Figure C. 1 Experiment setup.
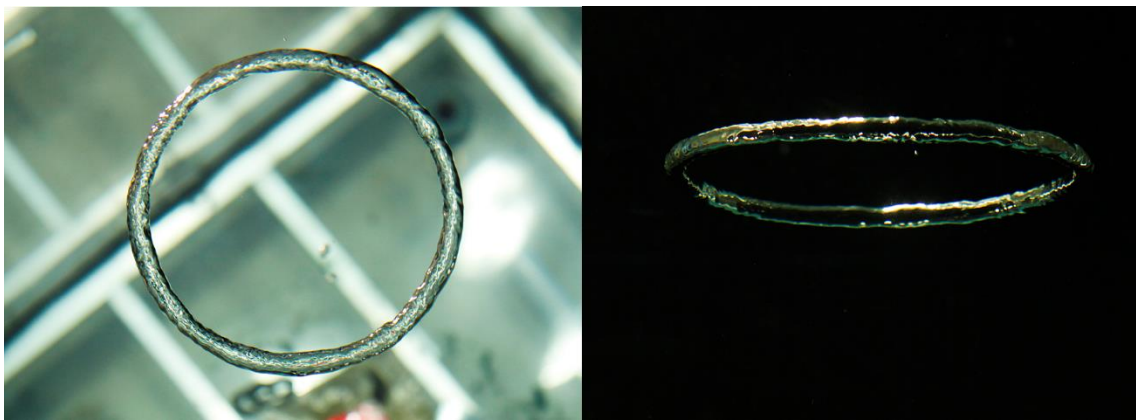
Figure C. 2 Buoyant vortex ring's image (Captured by Kristie Pearce).

The formation and translation of the laminar and turbulent vortex rings are shown in Figure C. 3. The surface of a laminar vortex ring is smooth, while that of the turbulent vortex ring develops a wavy unstable shape. The ring radius expands linearly with the

elevation, whether the bubble ring is laminar or turbulent. The expansion rate (dR/dz) of a

laminar ring is larger than that of a turbulent one. The rising velocity decreases as the ring

rises. In addition, the turbulent vortex ring forms at a higher location compared to a laminar

one.
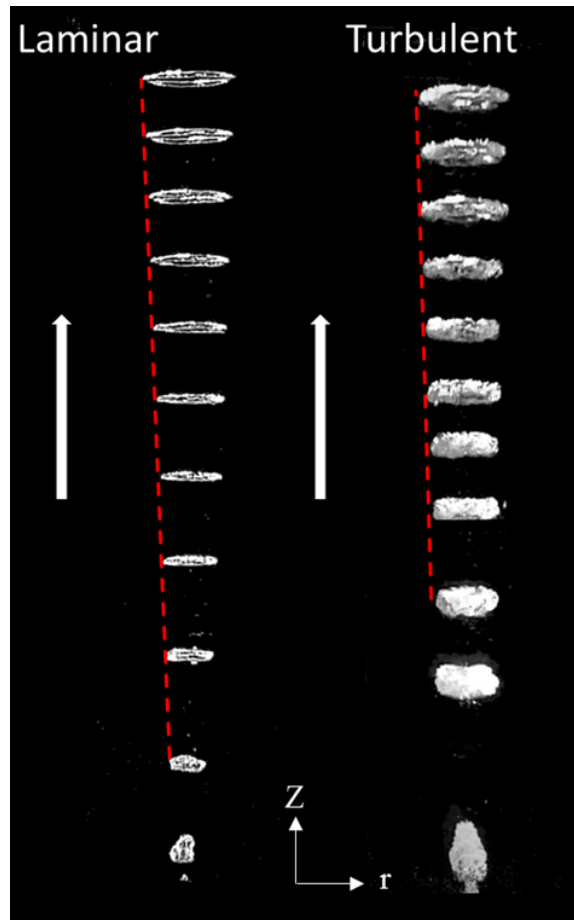
Figure C. 3 The formation and translation of the bubble ring at Bo=30 (laminar) and
Bo=379 (turbulent).

APPENDIX D: MATLAB PROGRAM FOR HOT-WIRE DATA

D. 1 Main Program

```
clc; clear all;

viscosity = 1.50635*10^-5; % viscosity of air at 20 degree

sample=1000000; %Sample Size

Fs=80000;      %Sample Frequency Hz

gain=1;              %Gain of the conditioner

offset=0;          %Offset of the conditioner

horizontal_number = 4; vertical_number = 47;

is_plot = 1;

U_infinite = 13.5;

C=[0.953954

0.356689

0.0846

0.000299

0.000176

];

U_mean = zeros(vertical_number, horizontal_number);

u_rms = zeros(vertical_number, horizontal_number);

skewness = zeros(vertical_number, horizontal_number);

flatness = zeros(vertical_number, horizontal_number);

Tu = zeros(vertical_number, horizontal_number);

U_relative = zeros(vertical_number, horizontal_number);
```

```
Tu_relative = zeros(vertical_number, horizontal_number);

dissipation_rate = zeros(vertical_number, horizontal_number);

kolmogorov_scale = zeros(vertical_number, horizontal_number);

integral_scale = zeros(vertical_number, horizontal_number);

taylor_scale = zeros(vertical_number, horizontal_number);

taylor_scale2 = zeros(vertical_number, horizontal_number);

vortexshedding_frequency = zeros(vertical_number, horizontal_number);

waitbar_denominator = horizontal_number * vertical_number;

waitbar_numerator = 0;

waitbar_name = waitbar(0, [int2str(waitbar_numerator) ' / ' int2str(waitbar_denominator)
' finished']);

zone = 1;

for index_h=4:horizontal_number;

     if index_h<10

         Horizontal = ['0' int2str(index_h)];

    else

        Horizontal =int2str(index_h);

    end


    for index_v=1:vertical_number;

        if index_v<10;

             Vertical = ['0' int2str(index_v)];

        else
```

```matlab
                Vertical = int2str(index_v);

         end

         name=[Horizontal Vertical];

         type='.txt';

         file=[name type];

         if exist(file,'file') == 2;

                E=importdata(file);      %load raw data

                U_instantaneous(:,1)=E.data(:,2);

                [U_mean(index_v,index_h), u_rms(index_v,index_h),

skewness(index_v,index_h), flatness(index_v,index_h), Tu(index_v,index_h), u] =

get_statistic(U_instantaneous);

                [U_relative(index_v,index_h), Tu_relative(index_v,index_h)] =

get_relative(U_infinite, U_mean(index_v,index_h), u_rms(index_v,index_h));

                dissipation_rate(index_v,index_h) =

get_dissipation(U_instantaneous,U_mean(index_v,index_h),Fs,sample,viscosity);

                kolmogorov_scale(index_v,index_h) =

get_kolmogorov(dissipation_rate(index_v,index_h),viscosity);

                integral_scale(index_v,index_h) =

get_integral_scale(U_mean(index_v,index_h), u, Fs);

                taylor_scale(index_v,index_h) =

get_taylor_scale(U_mean(index_v,index_h), u, Fs);
```

```matlab
                taylor_scale2(index_v,index_h) = (15 * viscosity * mean(u.^2) /

dissipation_rate(index_v,index_h))^0.5;

                vortexshedding_frequency(index_v,index_h) =

get_vortexsheddingfrequency(u, name, is_plot);

                clear E U_instantaneous u;

        end

        waitbar_numerator = waitbar_numerator + 1;

        waitbar(waitbar_numerator / waitbar_denominator, waitbar_name,

[int2str(waitbar_numerator) ' / ' int2str(waitbar_denominator) ' finished']);

    end

end

results(:,1) = U_mean(:);    results(:,2) = u_rms(:);

results(:,3) = skewness(:);    results(:,4) = flatness(:);

results(:,5) = Tu(:);    results(:,6) = U_relative(:);

results(:,7) = Tu_relative(:);    results(:,8) = dissipation_rate(:);

results(:,9) = kolmogorov_scale(:);    results(:,10) = integral_scale(:);

results(:,11) = taylor_scale(:);    results(:,12) = taylor_scale2(:);

results(:,13) = vortexshedding_frequency(:);

variable =

[{'U_mean'},{'u_rms'},{'skewness'},{'flatness'},{'Tu'},{'U_relative'},{'Tu_relative'},{'dis

sipation_rate'},{'kolmogorov_scale'},{'integral_scale'},{'taylor_scale'},{'taylor_scale2'},{

'vortexshedding_frequency'}];

results_plot = [variable;num2cell(results)];
```

D. 2 Subprograms

1. get_autoCorrCoef

```
function [rho_tau,tau]=get_autoCorrCoef(u,Fs)

N=length(u);

if N>2500000

    disp('Sample Number should not exceed 2500000');

    return

else

    d=N:-1:1;

    x=xcorr(u);

    x=x(N:length(x));%trancate the symmetrical part

    Rx_tau=x./d';

    Rx_0=mean(u.^2); %rho_tau=Rx_tau/Rx_0 where rho is a coefficient

    rho_tau=Rx_tau/Rx_0;

end

tau=(0:N-1)/Fs;
```

2. get_dissipation

```
function diss_rate = get_dissipation(U_instantaneous,mu,Fs,sample,v)

    U = 0;

    for i = 1 : sample-1;

        U = U + ((U_instantaneous(i+1)-U_instantaneous(i))*Fs)^2;

    end

    diss_rate = 15 * v / mu^2 /sample * U;
```

3. get_energyspectrum

```
function [] = get_energyspectrum(U_mean, dissipation_rate)

figure;

frequency = 1:80000;

wavenumber = (frequency.* (2 * pi))./   U_mean;

energy = 0.56 * dissipation_rate^(2/3).* wavenumber.^(-5/3);

plot(frequency, energy);

set(gca,'XScale','log');
```

4. get_fft

```
function [frequency,amplitude,vortexshedding_frequency,vortexshedding_amplitude]=get_fft(u)

[amplitude,frequency] = pwelch(u,2^15,[],2^17,80000);

low = 1;

while frequency(low) < 10;

    low = low + 1;

end

high = low;

while frequency(high) < 1000;

    high = high + 1;

end

[vortexshedding_amplitude,index]=max(amplitude(low:high,1));

vortexshedding_frequency=frequency(index + low - 1);

end
```

5. get_integral_scale

```
function integral_scale = get_integral_scale(U_mean, u, Fs)

    [rho_tau,tau]=get_autoCorrCoef(u,Fs);

    k=1;

    while rho_tau(k+1)>0;      %if rho_tau is too small stop;

        k=k+1;

    end

    integral_time_scale = trapz(tau(1:k),rho_tau(1:k));

    integral_scale=integral_time_scale * U_mean;
```

6. get_kolmogorov

```
function kolmogorov_scale = get_kolmogorov(diss_rate,v)

    kolmogorov_scale = (v^3/diss_rate)^0.25;
```

7. get_relative

```
function [U_relative, Tu_relative] = get_relative(U_infinite, U_mean, u_rms)

    U_relative = U_mean / U_infinite;

    Tu_relative = u_rms / U_infinite;
```

8. get_statistic

```
function [U_mean, u_rms, skewness, flatness, Tu, u] =
get_statistic(U_instantaneous)

    U_mean = mean(U_instantaneous);          % time averaged velocity

    u = U_instantaneous-U_mean;              % fluctuation velocities

    u_rms = sqrt(mean(u.^2));                % rms velocity

    skewness = mean(u.^3) / u_rms^3;         % skewness factor
```

flatness = mean(u.^4) / u_rms^4;   % flatness factor

Tu = u_rms / U_mean;   % turbulence intensity

9. get_taylor_scale

function taylor_scale = get_taylor_scale(U_mean, u, Fs)

taylor_time_scale = (mean(2.* (u.^2)) / mean((diff(u).*Fs).^2))^0.5;

taylor_scale = taylor_time_scale * U_mean;

10. get_vortexsheddingfrequency

function vortexshedding_frequency = get_vortexsheddingfrequency(u, name,

is_plot)

[frequency,amplitude,vortexshedding_frequency,vortexshedding_amplitude]=get_fft(u);

if is_plot == 1;

plot_vortexshedding(frequency,amplitude,vortexshedding_frequency,vortexshedding_am

plitude,name)

end

11. plot_vortexshedding

function

plot_vortexshedding(frequency,amplitude,vortexshedding_frequency,vortexshedding_am

plitude,name)

figure;

set(gcf,'visible','off');

frequency = frequency(1:round(length(frequency)/1));

amplitude = amplitude(1:round(length(amplitude)/1));

```matlab
plot(frequency,amplitude); %»æ³öNyquistÆµÂÊÖ®Ç°ËæÆµÂÊ±ä»¯µÄÕñ·ù
set(gca,'XScale','log')
hold on;
plot(vortexshedding_frequency,vortexshedding_amplitude,'o');
text(vortexshedding_frequency +
10,vortexshedding_amplitude,[num2str(round(vortexshedding_frequency)),'Hz']);
set(gca,'XScale','log');
xlabel('frequency/Hz');
ylabel('amplitude');
title('vortexshedding frequency');
grid on;
saveas(gcf, name,'jpg') % save plot
close(figure(gcf)) %close plot window
end
```

VITA AUCTORIS

NAME: Xueying Yan

PLACE OF BIRTH: Shenyang, Liaoning, China

YEAR OF BIRTH   1992

EDUCATION: Shenyang No. 2 High School, Shenyang, China,
                         2007-2010

                         Beijing University of Science and Technology,
                         Beijing, China,
                         2010-2014 B.Eng.

                         University of Windsor, Windsor, ON,
                         2015-2017 M.A.Sc.